PCCP

Implications for New Particle Formation in Air of the Use of Monoethanolamine in Carbon Capture and Storage

Journal:	*Physical Chemistry Chemical Physics*
Manuscript ID	CP-ART-01-2024-000316.R1
Article Type:	Paper
Date Submitted by the Author:	22-Feb-2024
Complete List of Authors:	Perraud, Veronique; University of California, Chemistry Roundtree, Kanuri; University of California, Chemistry Morris, Patricia; University of California, Chemistry Smith, James; University of California Irvine, Department of Chemistry Finlayson-Pitts, Barbara; University of California, Irvine, Department of Chemistry

Implications for New Particle Formation in Air of the Use of Monoethanolamine in Carbon Capture and Storage

Véronique Perraud,* Kanuri Roundtree, Patricia M. Morris, James N. Smith* and B. J. Finlayson-Pitts

[1]Department of Chemistry, University of California Irvine, Irvine, CA 92697

For submission to: *PCCP (Special Issues, 25th Anniversary)*

*Authors to whom correspondence should be addressed.

Email: vperraud@uci.edu; phone: (949) 824-2673; FAX (949) 824-2420

Email: jimsmith@uci.edu; phone: (949) 824-9518; FAX (949) 824-2420

keywords: monoethanolamine; water; methanesulfonic acid; thermal desorption chemical ionization mass spectrometry; new particle formation

Abstract

Alkanolamines are currently being deployed in carbon capture and storage (CCS) technology worldwide, and atmospheric emissions have been found to coincide with locations exhibiting elevated concentrations of methanesulfonic acid (MSA). It is thus critical to understand the fate and potential atmospheric reactions of these chemicals. This study reports the characterization of sub-10 nm nanoparticles produced through the acid-base reaction between gas phase monoethanolamine (MEA) and MSA, a product of organosulfur compound oxidation in air, using a flow reactor under dry and humid (up to ~60% RH) conditions. Number size distribution measurements show that MEA is even more efficient than methylamine in forming nanoparticles on reaction with MSA. This is attributed to the fact that the MEA structure contains both an -NH_2 and an -OH group that facilitate hydrogen bonding within the clusters, in addition to the electrostatic interactions. Due to this already strong H-bond network, water has a relatively small influence on new particle formation (NPF) and growth in this system, in contrast to MSA reactions with alkylamines. Acid/base molar ratios of unity for 4-12 nm particles were measured using thermal desorption chemical ionization mass spectrometry. The data indicate that reaction of MEA with MSA may dominate NPF under some atmospheric conditions. Thus, the unique characteristics of alkanolamines in NPF must be taken into account for accurate predictions of impacts of CCS on visibility, health and climate.

Introduction

Monoethanolamine ($HOCH_2CH_2NH_2$, MEA) is a multifunctional amine currently deployed in carbon capture and storage (CCS) technology systems aimed at sequestering CO_2 emissions before release into the atmosphere.[1-5] The most widely used CCS media is a 30% aqueous solution of monoethanolamine (MEA).[6] Briefly, the solvent medium chemically absorbs CO_2 contained in the flue gas, which leads to a CO_2-depleted gas stream exiting the stack. The solvent is subsequently regenerated and recycled back into the absorber column, while the CO_2 is compressed and captured. A potential drawback from these technologies is the likely release of MEA into the air.[4,5,7-14] For example, concentrations of MEA outside a CCS-equipped plant of the order of several ppb have been reported.[7] MEA is also used as a solvent in various consumer products and industrial processes.[15-19] In air, recognized fates of gas phase MEA to date include its reaction with O_3 and OH,[20-24] the formation of alkylaminium nitrate salts from its interaction with HNO_3[21,24] and acid-base reactions with gas phase and particulate sulfuric acid.[25,26]

Methanesulfonic acid (CH_3SO_3H, MSA) is a strong acid formed along with SO_2 (a sulfuric acid precursor) in the oxidation of dimethyl sulfide (DMS) and dimethyl disulfide (DMDS)[27-32] which have a variety of sources both natural and anthropogenic.[33-59] Therefore, it is not surprising that the oxidation product MSA is detected in the gas phase and in ambient particles worldwide. Ambient gas phase atmospheric concentrations of MSA range from mid-10^4 to 10^7 molecules cm^{-3}, and can reach levels similar to that of H_2SO_4, which is considered to be a major source of new particles.[60-69] In some instances, the MSA concentration in air can actually surpass that of

co-located H_2SO_4.[68,70] MSA has also been detected in ambient particles worldwide, including in marine and coastal environments,[71-77] in coastal areas affected by biomass burning plumes,[78,79] and near agricultural regions as well as near urban centers.[78,80,81] This acid has been detected in ultrafine and nucleation mode particles measured in the Arctic,[76,82-85] at urban sites[86,87] and in the Antarctic[88] as well as in a boreal forest.[67,89] Particulate MSA concentrations in the Arctic summertime have been observed to correlate well with new particle formation (NPF)[85,90-94] suggesting a role for MSA in the earliest stages of NPF and growth. Chen and co-workers[95] predicted that the total annual MSA budget would be 20 Gg S yr^{-1} from DMS oxidation reactions alone. However, climate change is dramatically modifying the extent of ice sheet coverage, exposing more sea water, which increases phytoplankton productivity and DMS emissions and thus MSA in air.[94,96-98] The significant contribution of MSA to atmospheric NPF is supported by both laboratory experiments[99-107] and quantum chemical calculations.[108-115]

Amines and MSA are both found in ambient particles.[67,80,116-118] This includes MEA, which has been detected as one of the most abundant amines in ambient particles in various locations around the globe,[119-124] overlapping with sources of both DMS and MSA. MEA has also been detected in biomass burning aerosols collected in St John, Newfoundland, Canada[125] and in both aerosol and precipitation samples over the North Atlantic Ocean.[126]

It is thought that NPF is responsible for a significant portion of the global cloud condensation nuclei budget.[127] In addition to influencing cloud properties, airborne particles are well known to interact with solar radiation, thus playing a critical role in the Earth's climate.[128,129] In a recent study, Hodshire et al.[130] predicted, using a simplified DMS oxidation

model, that inclusion of MSA formation and its role in aerosol processes (either acting as condensable non- or semi-volatile species, or participating in NPF) influenced the cloud-albedo aerosol indirect and the direct radiative effect.

While recent theoretical studies predicted that MEA may play an important role in NPF,[108] to date there have been no direct experimental investigations of particle formation from MEA and MSA. We present the first measurements of 4-12 nm nanoparticles formed from this reaction, including their size distributions as a function of time and relative humidity, as well as their size-resolved chemical composition. For comparison, some data for the reaction of MSA with methylamine (MA), which is known to efficiently form particles,[102,103,105,106] is also reported. It is shown that MEA is even more effective in forming new nanometer size particles than MA but surprisingly, is not very sensitive to the presence of water vapor. Such ultrafine particles are of particular concerns as they can be deposited deep into the respiratory tract and even cross cellular membranes to reach other organs.[131-136] Thus, this study has important implications for the potential impacts of CCS on climate,[128,129] visibility[137-140] and health.[131,132,136,141]

Experimental Methods

Flow Reactor Description. Particles were produced from the reaction of gas phase MSA with gas phase MEA (or MA) in the presence or absence of water vapor in a 1-m long borosilicate glass flow reactor[142] described in the Electronic Supplementary Information (ESI; Fig. S1).

Clean, dry air was provided by a purge air generator (Parker-Balston; model 75-62), and further purified by passing through carbon/alumina media (PermaPure, LLC) and a 0.01 μm inline filter (Parker Balston, BQ). Most of the air was supplied at the front end of the flow reactor through the perforated ring inlets as indicated in Fig. S1 (rings A, B and C). In experiments where water vapor was present, one or two bubblers filled with nanopure water (18.2 MΩ cm; Barnstead, Thermo Scientific) were used to humidify a fraction of the air introduced into the ring inlets. The bubblers were kept in a water bath to maintain a constant temperature of 22°C (295 K). Experiments were carried out at relative humidities (RH) up to ~60% as indicated by a humidity probe (Vaisala; model HMT 838) located at the end of the flow reactor. The reactants (MSA and MEA or MA) were introduced through the spoke inlets (spoke 2 and 3 respectively) located 60 cm downstream of the last ring inlet. The flow reactor was cleaned regularly with nanopure water and dried with clean hot air overnight (T = 343 K). After cleaning, the flow reactor was conditioned with gas-phase MSA for a least two days prior to an experiment. All experiments presented in this work were performed at 1 atm and at room temperature (T = 297 K).

Reactants. Liquid monoethanolamine ($NH_2CH_2CH_2OH$, Sigma Aldrich, >99.5%) was contained in a small 2-mL glass vial with a septum cap. Approximately ~1 cm of PEEK tubing (0.007" inner diameter) was inserted into the septum so that the MEA from the headspace diffused slowly into a stream of air. For comparison, parallel experiments were performed using MA (CH_3NH_2) with a commercial permeation tube (VICI Metronics). The amine vial (or permeation tube) was inserted into separate U-shaped glass tubes immersed into a water bath maintained at room temperature (T = 295 K). Glass beads were placed in the upstream arm of

the U-shaped glass tubes to provide high surface area to keep the gas flow at a constant temperature. Air flowed through each tube at a rate of 215 cm^3 min^{-1} for MEA and 93 or 211 cm^3 min^{-1} for MA. For MSA, air (53 to 216 cm^3 min^{-1}) flowed directly over the pure liquid (Sigma Aldrich, > 99.0%) contained in a glass trap which was maintained at room temperature using a water bath. Further details regarding the sampling, analysis and quantification of the gas phase reactants are given in the ESI (Text S1 and Fig. S2). The initial concentrations of the reactants after dilution in the flow reactor were (1.7-6.8) $\times$ 10^{10} molecules cm^{-3} for MSA (0.7-2.8 ppb), (3.7-8.1) $\times$ 10^{10} molecules cm^{-3} for MEA (1.5-3.3 ppb) and (11.8-26.6) $\times$ 10^{10} molecules cm^{-3} for MA (4.8-10.8 ppb). Note that these concentrations represent upper limits as they do not account for potential wall losses.

Particle size distribution measurements. Particle size distributions were continuously measured using a moveable stainless steel sampling line (O.D. 0.635 cm) located inside the flow reactor along the centerline and placed at distances ranging from 3 to 43 cm away from spoke 2 (i.e., the MSA addition port). All particle size distributions reported in this study are number size distributions, unless stated otherwise. These distances correspond to reaction times in the reactor ranging from 0.3 to 4.5 s (total flow rate 23.4 L min^{-1}) or 0.5 to 7.7 s (total flow rate 10.7 L min^{-1}) based on a conversion factor determined in previous studies.[99] Note that the amine addition port is introducing the reactant backward into the flow stream so that the reaction of MSA with MEA (MA) is occurring in between spoke 2 and 3, and we chose the MSA addition port as our t = 0 reaction time. It is expected that the residual reactants present in the stream exiting the flow reactor are lost to the walls of the small (ID 0.18 inches) sampling line. Therefore, the reaction times reported are those in the flow reactor, but these could be

underestimated if the reaction continues in the sampling line (residence time ~ 0.3-0.4 s) and the connection to the SMPS (residence time ~ 0.8 s). Particle losses through the sampling lines to the SMPS were accounted for as described in the ESI (Text S2; Fig. S3). The shortest reaction time accessible (i.e. 0.3 s or 0.5s depending on the total flow in the flow tube, that was 23.4 or 10.7 L min^{-1} respectively) is expected to be the most vulnerable to residence time artefacts. This was tested by sampling at different flow rates through the sampling line (2.4 to 4.8 L min^{-1}), for a given experiment conducted at 0.5 s. Results presented in Fig. S4 show no change in the size distribution measured at all flow rates and suggest that reaction in the sampling line is not significant.

Size distributions were measured using a scanning mobility particle sizer (SMPS) consisting of a ^{210}Po radioactive source (10 mCi; NRD LLC; model P-2021), an electrostatic classifier (model 3080; TSI Inc.) equipped with a nano-differential mobility analyzer (nano-DMA; model 3085; TSI, Inc.), and a butanol-based ultrafine condensation particle counter (UCPC; model 3776; TSI, Inc.). To prevent buildup of the reactants in the SMPS during sampling, the sheath air inside the DMA was not recirculated, but instead air was provided by the purge air generator (15 L min^{-1}) and a vacuum pump connected to the sheath air flow pulled the sheath air out of the DMA. The aerosol flow was set to 1.5 L min^{-1}, which provided measurements of the size distributions over a mobility diameter range of 2.5 to 64 nm. The software AIM v9 (TSI, Inc.) was used to record and process the data. Particles were observed to be stable for long periods of time (Fig. S5), allowing for size-resolved measurements that took up to 20 min per scan to yield enough mass for mass spectrometric analysis.

Size-resolved chemical composition measurements. Nanoparticles with diameters ranging from 4 to 12 nm were sampled using a thermal desorption chemical ionization mass spectrometer (TDCIMS) [105,143-146] which was connected to the same sampling line as the SMPS. The particle stream was sampled through two inlets, each equipped with a ^{210}Po unipolar charger (UPC)[143,147] to generate negatively charged particles. At each inlet, particles were subsequently size-selected using a radial nano-DMA (rDMA) running in either high resolution mode with a sheath flow of 10 L min^{-1} and an aerosol flow of 1.0 L min^{-1} through each nano-rDMA, or low resolution mode with a sheath air flow of 5.0 L min^{-1} and an aerosol flow rate of 1.6 L min^{-1} through each nano rDMA.[148] For both conditions, instead of recirculating the sheath gas within the nano-DMA, gaseous N_2 produced from the headspace of a liquid N_2 dewar was used as the sheath flow to prevent the accumulation of gas-phase MSA or MEA, and a vacuum pump was used at the DMA sheath flow outlet. The particles were collected on the tip of a Pt filament by electrostatic precipitation (applied high voltage of +3.5 kV). The filament was continuously flushed with an additional 1.25 L min^{-1} flow of N_2 to minimize sampling artifacts from gas-phase species. To select particles with a defined mobility diameter, the voltage on each rDMA was varied from 30 to 325 V. Note that the use of two separate inlets, which merged at the collection wire region, increases the flux and mass of particles that are collected on the wire without sacrificing the rDMA resolution.

The TDCIMS was run in positive ion mode to measure MEA with $(H_2O)_nH^+$ as the reagent ions (n=0–3), and in negative ion mode to measure MSA with $(H_2O)_nO_2^-$ as the reagent ions from the presence of trace amounts of H_2O and O_2, respectively, in the carrier N_2 gas. Monoethanolamine was detected as two major ions in the mass spectra, the parent $[M+H]^+$ ion

(*m/z* 62) and a fragment ion corresponding to $[M+H-H_2O]^+$ (*m/z* 44). The fragmentation of the parent $[M+H]^+$ ion of MEA is consistent with early experimental and theoretical studies[149,150] showing that although the amino group is the favored protonation site due to its higher proton affinity compared to the alcohol group,[151] rearrangement and the loss of H_2O dominates over the loss of NH_3. The corresponding fragment ion associated with the loss of NH_3 (*m/z* 45) was not observed in any of the mass spectra. MSA was detected in negative ion mode as the parent deprotonated $[M-H]^-$ ion (*m/z* 95) followed by a major fragment ion at *m/z* 80 (SO_3^-), with additional minor ions at *m/z* 64 (SO_2^-), *m/z* 96 (SO_4^-), *m/z* 97 $(HSO_4)^-$ and *m/z* 112 (SO_5^-). Both positive and negative mass spectra are presented in Fig. S6. From the desorption profiles presented in Fig. S7, it is evident that MEA (and MA; data not shown) desorbs first from the filament followed by MSA, consistent with the differences in their respective saturation vapor pressures (P_{sat}) at 298 K: $P_{sat}(MEA) = 3.4 \times 10^{-4}$ atm[152] and $P_{sat}(MSA) = 7.4 \times 10^{-7}$ atm.[153] Additional details on the TDCIMS analysis are described in the ESI (Text S3-S5; Fig. S6-S11).

Results and Discussion

Figure 1 represents the size distributions of particles from the MSA+MEA reaction under dry conditions, with each panel (A-F) representing a different reactant concentration condition. Varying reactant concentrations was achieved by either increasing or decreasing the flow of the reactant that was introduced into the flow tube, or by changing the total flow rate in the flow tube (23.4 L min^{-1} for Panels (A-C); 10.7 L min^{-1} for panels (D-F)). Clearly, mixing gas phase MSA and MEA at low ppb levels results in rapid formation of particles. Corresponding plots of the

191 evolution of the total number concentration as well as the geometric diameter as a function of the
192 reaction time are presented in Fig. S12. Even at the smallest reactant concentrations (Fig. 1A,
193 1.5 ppb MEA, 0.68 ppb MSA), particles measured at the shortest distance (t = 0.3 s; total flow
194 rate 23.4 L min^{-1}) are formed at a number concentration of 6.3 $\times 10^6$ particles cm^{-3} with a
195 geometric mean mobility diameter (GMD) of ~ 4 nm. At 2.4 s, the number concentration
196 increases by a factor of two with little change in size. At longer times, there is no further
197 increase in the particle number concentration while the particles continue to grow to a GMD of
198 ~4.6 nm, suggesting that under these conditions there is a balance between nucleation, growth by
199 addition of the reactants onto particles, and coagulation. Particle losses inside the flow tube were
200 estimated using the particle loss calculator tool developed by von der Weinder et al.[154] (using a
201 density of 1 g cm^{-3}), and was found to be small for all diameters (e.g. for a particle diameter of
202 2.5 nm, particle transmission is predicted to be 92 or 95% for a total flow rate inside the flow
203 tube of 10.7 or 23.4 L min^{-1}).

204 Similar behavior is seen as the initial MSA concentration is increased, but with larger
205 total particle number concentrations formed (Fig. 1B,C; Fig. S12 A,B). In this case, at longer
206 reaction times the particle number concentrations start to decrease and the GMD increases due to
207 coagulation (Fig. 1C). Similar, but more pronounced, trends are seen at an initial MEA
208 concentration of 3.3 ppb and increasing MSA concentrations (Fig. 1D-F). For approximately the
209 same MSA concentration (Fig. 1B and 1D; Fig. 1C and 1E), doubling the concentration of MEA
210 leads to an increase in total number concentration of a factor of ~1.2-1.4 at 2.3-2.4 s reaction
211 time, with an increase in diameter from 4.9 to 5.6 nm (MSA = 1.4-1.5 ppb) and from 5.3 to 6.3
212 nm (MSA = 2.8-3.0 ppb).

For the low concentration series, the formation of approximately half of the peak particle concentration at the first measurement time implies that the rate-determining step is fast. There is some uncertainty in the exact reaction time for this first data point since it does not take into account possible continued reaction in the sampling lines. However, a half-life of ~ 0.5 s for the reaction of MSA with excess MEA at 1.5 ppb (Fig. 1A), is consistent with a gas phase bimolecular rate constant for MEA with MSA of approximately 4×10^{-11} cm^3 $molecule^{-1}$ s^{-1}.

The particle formation rate ($J_{>2.5nm}$) was estimated using the total concentration of particles measured at ~2.4 s (peak concentration) for all conditions, and dividing by 2.4 s. Figure 2 shows the resulting $J_{>2.5nm}$ values as a function of the product of the MEA and MSA initial concentrations. There is an initial rapid increase which is approximately linear out to [MEA] × [MSA] ~ 2 ppb^2, suggesting that the initial 1:1 cluster formation is the rate-determining step. The drop-off at higher concentrations reflects coagulation. This is consistent with the TDCIMS measurements (Fig. 3), which show that the acid/base molar ratios in the particles from 4-12 nm remains within experimental error of one. All measurements were performed at 4.5 s reaction time, and at [MEA] initial concentration of 1.5 ppb, and there were no significant differences in the measured molar ratio across the experiments performed under excess MEA ([MSA] = 0.68 ppb), pseudo-equimolar MEA/MSA ([MSA] = 1.4 ppb) or excess MSA ([MSA]= 2.8 ppb), thus the data obtained for all [MSA] concentrations was averaged together.

MSA concentrations in air can be as high as 10^7 molecules cm^{-3} (~0.4 ppt)[60,61,66,68] and MEA in the low ppb range has been recorded outside a CCS facility.[7] The slope of the line in

Fig. 2 at the lowest reactant concentrations is (5.3 ± 0.03) × 10^6 particles cm^{-3} ppb^{-2} so a NPF rate from the upper limit atmospheric concentrations of MEA (10 ppb) and MSA (0.4 ppt) of as much as ~21,200 particles cm^{-3} is predicted. This can be compared to a range of formation rates of particles >3 nm diameter (J_3) from sulfuric acid of 0.001 – 10^5 cm^{-3} observed in different environments around the world.[155] In short, even for conditions where MEA and MSA concentrations are less than the reported maxima, this single reaction system may contribute significantly to NPF and its importance may increase as MEA use in CCS increases.

Efficient particle formation from MEA and MSA is consistent with the excellent stability at room temperature and low vapor pressure of the MSA-MEA salt synthesized by Greaves and co-workers.[156] Furthermore, MEA-MSA has been reported to have properties of a protic ionic liquid, even though it remains a solid at room temperature.[156-159] Its properties include a glass transition of -44 °C, melting point of about 100 °C, and a thermal stability up to 286-323 °C for the fused salt.[156]

Tropospheric air contains significant amounts of water vapor, hence the impact of relative humidity (RH) on particle formation from MEA + MSA was also examined. Surprisingly, and in contrast to previous results obtained for small alkylamines, the addition of water vapor to the MSA+MEA system did not significantly increase the number concentration at RH below ~ 20% as indicated in Fig. 4. Figure 5A,B shows the evolution of the particle size distributions as a function of time at an RH of ~50% for two different sets of precursor concentrations corresponding to the dry conditions presented in Fig. 1A and 1C respectively. The evolution of the size distributions as a function of time in the flow reactor is similar to that

observed under dry conditions. To better compare the dry versus humid case, total particle concentrations and geometric mean diameters measured at 4.5 s over several repeated experiments were averaged and are shown in Fig. S13. The addition of water vapor increased the total number concentration by about only a factor of 1.3-1.5 as indicated by the bars. Note that the enhancement factor (EF) measured at 4.5 s for the high MSA, high RH case is an underestimate as it already includes coagulation (Fig. 5C). At the peak particle concentration (t = 1.4 s reaction time), EF = 1.9. There is only a small increase in size (red squares) at the highest MSA concentrations.

Classical nucleation theory predicts that the number of water molecules in the critical cluster can, under some conditions, be obtained from the slope of a log-log plot of the formation rate of new particles versus the gas phase water concentration.[160] However, this is highly dependent on a number of assumptions.[161] As seen in Figure 6, there is no significant correlation with H_2O concentration. This could indicate that water is not a central ingredient in the critical cluster formed from MEA and MSA. Alternatively, it could be due to the absence of an energy barrier in the reaction so the slope simply reflects a lack of particle formation rate on the water concentration.[161] Furthermore, no change in the acid/base molar ratio was observed in the TDCIMS measurements in the presence of water compared to the dry case (Fig. 3; blue data points) indicating that the particles remained neutral. This lack of dependence on water is in contrast to previous results obtained for the small alkylamines,[102] where a slope of 1.3-2.3 in the log-log plot was observed.

Shen et al.[108] carried out computational studies of cluster formation from MEA and MSA, They showed that the 1:1 cluster was the least stable and hence formation of this cluster is the rate-determining step. This is consistent with the measured rates of particle formation depending on the product of the MEA and MSA concentrations and the 1:1 acid/base ratio of the particles. They demonstrated that the binding of MEA and MSA was determined by a combination of proton transfer from the acid MSA to the nitrogen of the MEA base, along with hydrogen bonding. MEA differs from simple amines in that it has both the $-NH_2$ group as well as the -OH group, providing more than one hydrogen-bonding opportunity to MSA. Indeed, in all acid-base clusters, MSA acted as a H-bond donor and in many of the clusters, the -OH group of MEA acted as a H-bond donor to MSA. This results in strongly bound clusters held together by both electrostatic forces and a network of H-bonds, as illustrated in Fig. S14. It is interesting that the resulting structures have the $-CH_3$ group of MSA on the edge of the cluster, making the cluster somewhat hydrophobic. The hydrate distribution reported by Shen et al.[108] predicted that each cluster was predominantly hydrated by only one water molecule even at relatively high RH (80%). They also predicted that if water is present during cluster formation, it will enhance particle formation by about an order of magnitude at 50% RH due to a decrease in the evaporation rate of the initially formed 1:1 cluster. This predicted increase is significantly greater than the factor of 1.5-1.6 measured in these experiments.

In previous studies of NPF from MSA and amines, methylamine (MA) was shown to be the most efficient of the simple alkylamines in forming particles.[102,103,105,106] Figure 7 compares the size distributions of particles formed from the reactions of 1.4 ppb MSA with 1.5 ppb MEA or 4.8 ppb MA under dry conditions. Even with three times the amine concentration, the total

297 concentration of particles formed from MA is 17 times smaller than from MEA. This is
298 consistent with previously reported theoretical calculations[108,114,162] which predict a greater
299 stability of the clusters with the increased H-bonding capability of MEA and, as a consequence,
300 particle formation rates that are orders of magnitude higher for MSA+MEA compared to that for
301 MSA+MA at similar concentrations. The gas phase basicity[151] of MEA (896.8 kJ mol^{-1})
302 compared to MA (864.5 kJ mol^{-1}) also favors particle formation from MEA, along with the
303 increased H-bonding opportunities.

304 In previous experimental studies, water had a dramatic effect on NPF from MSA reacting
305 with small alkylamines,[102,104-106,163] quite different from MEA. In the case of MA, the presence
306 of water during particle formation led to a large increase in both number concentration and size
307 starting at RH < 10% (Fig. S15). Calculations indicated that the 4MSA-4 MA cluster with one
308 water molecule, for example, resulted in a structure that had many potential hydrogen bonding
309 sites available, allowing the cluster to grow via H-bonding with other species.[163] For MEA,
310 however, the clusters already have strongly hydrogen-bonded internal networks so that
311 opportunities for further interactions with water molecules are reduced.

312 To compare the relative importance of the MEA and MA reactions with MSA for particle
313 formation under atmospheric conditions, measurements under 10-50% RH were carried out with
314 MA (Fig. S15). Figure 8 shows the NPF rate ($J_{>2.5nm}$) for MEA compared to that of MA as a
315 function of the product of the reactant concentrations. The slope of the linear fit through the data
316 for the MEA reaction is more than four times that of the MA reaction. Thus, although NPF from
317 MA + MSA is greatly enhanced in the presence of water, the MEA reaction is still more efficient

under similar conditions. This highlights the significance of alkanolamines in NPF at low concentrations and points to H-bonding as a driver for NPF with MSA.

Conclusions

This study shows that the acid-base interaction of a short chain alkanolamine, MEA, used in CCS with MSA is quite strong and produces sub-10 nm particles extremely efficiently compared to a simple primary alkylamine, methylamine. Water vapor has a limited impact on NPF rates as MEA has OH- groups that already promote strong H-bonding network within the clusters. This is in contrast with previous work on alkylamines where water had a large impact on nucleation and growth of new particles. The particle composition from 4 - 12 nm showed an acid/base molar ratio close to unity, whereas those from the MA reaction contained more acid at the smaller diameters. These findings highlight that there is not a one-size-fits-all when it comes to treating amine interactions with MSA in atmospheric models.

The overall contribution of MSA-initiated aerosol chemistry may become increasingly more important in the future.[164] For example, there is a reduction of sea-ice coverage at the poles, leading to an increase in DMS emissions[94,96-98] with an associated increase in MSA. At the same time, there has been a decline in anthropogenic SO_2 emissions over few the past decades,[165-170] with a related reduction in particulate sulfate in ambient particles in the Northern part of the globe.[167,168,171,172] Thus, MSA acid-base mediated NPF will become increasingly more important in air in the near future.

Lastly, alkanolamines are being widely deployed as in CCS technology which may lead to an increase in their abundance in the atmosphere. Thus, assessing and understanding the impacts of this acid-base driven chemistry on new particle formation in air is more important than ever.

Acknowledgments

The authors are grateful to the National Science Foundation (Grants No. 1928252 and CHE-2004066) and the Army Research Office (Grant No. W911NF2010064) for supporting this research. K. R. acknowledges support from the Lucille Foundation and the Chemistry Summer Undergraduate Research Fellowship (Chem-SURF). The authors thank Dr. Paulus Bauer for helpful discussions during the preparation of this manuscript. The authors are also grateful to Dr. Natalia Karimova and Dr. R. Benny Gerber for their assistance in the DFT calculations and access to the Green-Planet Cluster at the University of California, Irvine.

Electronic Supplementary Information

The supporting information material is available free of charge on the ACS Publications website. It includes supporting texts covering additional details on the experimental methods as well as 15 figures (S1-S15).

357

358 # ORCID numbers

V. Perraud	0000-0003-1247-9787
K. Roundtree	0009-0001-0013-3394
P. M. Morris	0009-0008-6823-6569
J. N. Smith	0000-0003-4677-8224
B. J. Finlayson-Pitts	0000-0003-4650-168X

359

Figure Captions

Figure 1. Size distributions of particles from MEA (1.5 ppb) reacting with (A) 0.68 ppb MSA, (B) 1.4 ppb MSA and (C) 2.8 ppb MSA, and size distribution from MEA (3.3 ppb) reacting with (D) 1.5 ppb MSA, (E) 3.3 ppb MSA and (F) 6.1 ppb MSA. Measurements were conducted at the same sampling ports distributed equally along the length of the flow tube, but experiments displayed in panel (A-C) were performed with a total flow rate of 23.4 L min^{-1} (resulting in reaction times between 0.3 and 4.5 s), while experiments displayed in panel (D-F) were performed with a total flow rate of 10.7 L min^{-1} (resulting in reaction times between 0.5 and 7.7s). All experiments were performed under dry conditions, and size distributions are the average of 3 to 8 replicates (error bars correspond to one standard deviation) for each reaction time. All size distributions were corrected for particle losses through the sampling lines. Total particle concentrations and geometric mean diameters as a function of reaction times are given in Fig. S12.

Figure 2. Particle formation rate ($J_{>2.5\ nm}$) for the MSA+MEA system under dry conditions as a function of the product of the MSA and MEA mixing ratios in ppb. Each data point represents an average over 3 to 8 individual SMPS scans taken at 2.3-2.4 s reaction time, with error bars representing one standard deviation, and corrected for particle losses through the sampling lines. The red line is a linear fit to the data ([MSA] $\times$ [MEA] $\leq$ 2 ppb^2) with a slope of (5.3 $\pm$ 0.03) $\times$ 10^6 particles cm^{-3} ppb^2.

Figure 3. Acid/base molar ratio measured by the TDCIMS for the MSA+MEA system, under dry conditions (red data points) and at 52% RH (blue data points) measured at 4.5 s reaction time. MEA was measured in POS ion mode while MSA was measured in NEG ion mode, and the ion distributions in the MS spectra were similar at all reactant concentrations (Fig. S6). Text S5 provides more detailed information on how the acid/base molar ratios were estimated. All measurements were performed with initial MEA concentration of 1.5 ppb. No significant difference was observed in the measured molar ratio across for experiments performed with [MSA] = 0.68 ppb, [MSA] = 1.4 ppb or [MSA] = 2.8ppb, in either dry or humid conditions; thus the data points represent average values across the [MSA] concentrations range for each RH condition. For each data point, the error bars represent one standard deviation. The dashed line corresponds to an acid/base molar ratio of unity for reference.

Figure 4. Evolution of the particle size distributions as a function of relative humidity (RH) from the reaction of MSA (0.7 ppb) with MEA (1.4 ppb). Panel (A) represents the evolution as a function of time while panel (B) represents a snapshot of the size distributions at a given RH (each distribution is an average over three SMPS scans with the error bars representing one

standard variation). All measurements were performed at 4.5 s reaction time, and particle size distributions were corrected for particle loss through the sampling lines.

Figure 5. Size distributions (A and B) and evolution of the particle total concentrations and geometric mean diameters measured as a function of the reaction time (C and D) in the flow reactor for the MSA+MEA reaction system at 50% RH. All lines in panels C and D are guides to the eye. All data originate from replicate scans (n = 5) and are displayed with one standard deviation. All size distributions were corrected for particle losses through the sampling lines.

Figure 6. Logarithm of the particle formation rate ($J_{>2.5\ nm}$) for the MSA+MEA system under humid conditions (RH ranging from 8 to 56%) as a function of the log of the water concentration (in molecule cm^{-3}). Each data point represents an average over 3 to 6 individual SMPS scans taken at 4.5 s reaction time, with error bars representing one standard deviation. All data points were corrected for particle loss through the sampling line. Red data are for [MSA] = 0.68 ppb and [MEA] = 1.5 ppb while the blue data are for [MSA] = 2.8 ppb and [MEA] = 1.5 ppb. The slopes of the lines are 0.04 for 2.8 ppb MSA and 0.2 for 0.68 ppb MSA.

Figure 7. Representative averaged size distribution (red trace) from the reaction of MSA (1.4 ppb) with MEA (1.5 ppb). For comparison, a size distribution for MSA (1.4 ppb) reacting with MA (4.8 ppb) is also shown (green trace). Both size distributions were taken at ~4 s reaction time. Each size distribution was averaged over five consecutive scans and the shaded area corresponds to one standard deviation uncertainty. The thick line corresponds to a log normal fit to the averaged data. Both size distributions have been corrected for particle losses through the sampling lines.

Figure 8. Comparison between particle formation rate ($J_{>2.5\ nm}$) for the MSA+MEA and the MSA+MA systems under humid conditions (RH ranging from 8 to 56%) as a function of the product of the MSA and the amine mixing ratios in ppb. Each data point represents an average over 3 to 6 individual SMPS scans taken at 4.5 s reaction time, with error bars representing one standard deviations. The dashed lines are exponential fits to the data and the solid lines are the tangent to the fits with slopes of 5.5×10^6 and 1.2×10^6 for the MSA+MEA and MSA+MA systems respectively. All data points were corrected for particle loss through the sampling lines.

References

1. G. T. Rochelle, Amine Scrubbing for CO_2 Capture, *Science,* 2009, **325**, 1652-1654.
2. C. H. Yu, C. H. Huang, C. S. Tan, A review of CO_2 capture by absorption and adsorption, *Aerosol Air Qual. Res.,* 2012, **12**, 745-769.
3. S. A. Mazari, B. S. Ali, B. M. Jan, I. M. Saeed, S. Nizamuddin, An overview of solvent management and emissions of amine-based CO_2 capture technology, *Int. J. Greenh. Gas Con.,* 2015, **34**, 129-140.
4. L. Cuccia, J. Dugay, D. Bontemps, M. Louis-Louisy, J. Vial, Analytical methods for the monitoring of post-combustion CO_2 capture process using amine solvents: A review, *Int. J. Greenh. Gas Con.,* 2018, **72**, 138-151.
5. M. Corsten, A. Ramirez, L. Shen, J. Koornneef, A. Faaij, Environmental impact assessment of CCS chains - Lessons learned and limitations from LCA literature, *Int. J. Greenh. Gas Con.,* 2013, **13**, 59-71.
6. M. Akram, K. Milkowski, J. Gibbins, M. Pourkashanian, Comparative energy and environmental performance of 40 % and 30 % monoethanolamine at PACT pilot plant, *Int. J. Greenh. Gas Con.,* 2020, **95**, ARTN 102946, doi: 102910.101016/j.ijggc.102019.102946.
7. L. Zhu, G. W. Schade, C. J. Nielsen, Real-time monitoring of emissions from monoethanolamine-based industrial scale carbon capture facilities, *Environ. Sci. Technol.,* 2013, **47**, 14306-14314.
8. J. Mertens, J. Knudsen, M. L. Thielens, J. Andersen, On-line monitoring and controlling emissions in amine post combustion carbon capture: A field test, *Int. J. Greenh. Gas Con.,* 2012, **6**, 2-11.
9. J. Mertens, H. Lepaumier, D. Desagher, M. L. Thielens, Understanding ethanolamine (MEA) and ammonia emissions from amine based post combustion carbon capture: Lessons learned from field tests, *Int. J. Greenh. Gas Con.,* 2013, **13**, 72-77.
10. E. F. da Silva, H. Kolderup, E. Goetheer, K. W. Hjarbo, A. Huizinga, P. Khakharia, I. Tuinman, T. Mejdell, K. Zahlsen, K. Vernstad, A. Hyldbakk, T. Holten, H. M. Kvamsdal, P. van Os, A. Einbu, Emission studies from a CO_2 capture pilot plant, *Energy Procedia,* 2013, **37**, 778-783.
11. J. Fagerlund, R. Zevenhoven, J. Thomassen, M. Tednes, F. Abdollahi, L. Thomas, C. J. Nielsen, T. Mikoviny, A. Wisthaler, L. Zhu, C. Biliyok, A. Zhurkin, Performance of an amine-based CO_2 capture pilot plant at the Fortum Oslo Varme Waste to Energy plant in Oslo, Norway, *Int. J. Greenh. Gas Con.,* 2021, **106**, Art No 103242.
12. M. X. Fang, N. T. Yi, W. T. Di, T. Wang, Q. H. Wang, Emission and control of flue gas pollutants in CO_2 chemical absorption system - A review, *Int. J. Greenh. Gas Con.,* 2020, **93**, Art No 102904.
13. A. K. Morken, B. Nenseter, S. Pedersen, M. Chhaganlal, J. K. Feste, R. B. Tyborgnes, O. Ullestad, H. Ulvatn, L. Zhu, T. Mikoviny, A. Wisthaler, T. Cents, O. M. Bade, J. Knudsen, G. de Koeijer, O. Falk-Pedersen, E. S. Hamborg, Emission results of amine plant operations from MEA testing at the CO_2 Technology Centre Mongstad, *Energy Procedia,* 2014, **63**, 6023-6038.

14. K. Veltman, B. Singh, E. G. Hertwich, Human and environmental impact assessment of postcombustion CO_2 capture focusing on emissions from amine-based scrubbing solvents to air, *Environ. Sci. Technol.,* 2010, **44**, 1496-1502.
15. M. M. Fiume, B. A. Heldreth, W. F. Bergfeld, D. V. Belsito, R. A. Hill, C. D. Klaassen, D. C. Liebler, J. G. Marks, R. C. Shank, T. J. Slaga, P. W. Snyder, F. A. Andersen, Safety assessment of ethanolamine and ethanolamine salts as used in cosmetics, *Int. J. Toxicol.,* 2015, **34**, 84s-98s.
16. B. C. McDonald, J. A. de Gouw, J. B. Gilman, S. H. Jathar, A. Akherati, C. D. Cappa, J. L. Jimenez, J. Lee-Taylor, P. L. Hayes, S. A. McKeen, Y. Y. Cui, S. W. Kim, D. R. Gentner, G. Isaacman-VanWertz, A. H. Goldstein, R. A. Harley, G. J. Frost, J. M. Roberts, T. B. Ryerson, M. Trainer, Volatile chemical products emerging as largest petrochemical source of urban organic emissions, *Science,* 2018, **359**, 760-764.
17. J. Wooley, W. W. Nazaroff, A. T. Hodgson, Release of ethanol to the atmosphere during use of consumer cleaning products, *J. Air Waste Manage. Assoc.,* 1990, **40**, 1114-1120.
18. X. Ge, A. S. Wexler, S. L. Clegg, Atmospheric amines - Part I. A review, *Atmos. Environ.,* 2011, **45**, 524-546.
19. J.-A. Seo, I.-H. Bae, W.-H. Jang, J.-H. Kim, S.-Y. Bak, S.-H. Han, Y.-H. Park, K.-M. Lim, Hydrogen peroxide and monoethanolamine are the key causative ingredients for hair dye-related dermatitis and hair loss, *J. Dermatol. Sci.,* 2012, **66**, 12-19.
20. N. Borduas, J. P. D. Abbatt, J. G. Murphy, Gas phase oxidation of monoethanolamine (MEA) with OH radical and ozone: kinetics, products, and particles, *Environ. Sci. Technol.,* 2013, **47**, 6377-6383.
21. M. Karl, C. Dye, N. Schmidbauer, A. Wisthaler, T. Mikoviny, B. D'Anna, M. Muller, E. Borras, E. Clemente, A. Munoz, R. Porras, M. Rodenas, M. Vazquez, T. Brauers, Study of OH-initiated degradation of 2-aminoethanol, *Atmos. Chem. Phys.,* 2012, **12**, 1881-1901.
22. L. Onel, M. A. Blitz, P. W. Seakins, Direct determination of the rate coefficient for the reaction of OH radicals with monoethanol amine (MEA) from 296 to 510 K, *J. Phys. Chem. Lett.,* 2012, **3**, 853-856.
23. C. J. Nielsen, B. D'Anna, C. Dye, M. Graus, M. Karl, S. King, M. M. Maguto, M. Muller, N. Schmidbauer, Y. Stenstrom, A. Wisthaler, S. Pedersen, Atmospheric chemistry of 2-aminoethanol (MEA). *Energy Procedia,* 2011, **4**, 2245-2252.
24. S. M. Murphy, A. Sorooshian, J. H. Kroll, N. L. Ng, P. Chhabra, C. Tong, J. D. Surratt, E. Knipping, R. C. Flagan, J. H. Seinfeld, Secondary aerosol formation from atmospheric reactions of aliphatic amines, *Atmos. Chem. Phys.,* 2007, **7**, 2313-2337.
25. X. M. Tian, Y. X. Chu, C. K. Chan, Reactive uptake of monoethanolamine by sulfuric acid particles and hygroscopicity of monoethanolaminium salts, *Environ. Sci. Tech. Let.,* 2022, **9**, 16-21.
26. H. B. Xie, J. Elm, R. Halonen, N. Myllys, T. Kurten, M. Kulmala, H. Vehkamaki, Atmospheric fate of monoethanolamine: enhancing new particle formation of sulfuric acid as an important removal process, *Environ. Sci. Technol.,* 2017, **51**, 8422-8431.
27. B. Rosati, S. Christiansen, R. W. de Jonge, P. Roldin, M. M. Jensen, K. Wang, S. P. Moosakutty, D. Thomsen, C. Salomonsen, N. Hyttinen, J. Elm, A. Feilberg, M. Glasius,

M. Bilde, New particle formation and growth from dimethyl sulfide oxidation by hydroxyl radicals, *ACS Earth Space Chem.,* 2021, **5**, 801-811.

28. P. Van Rooy, R. Drover, T. Cress, C. Michael, K. L. Purvis-Roberts, P. J. Silva, M. J. Nee, D. Cocker, Methanesulfonic acid and sulfuric acid aerosol formed through oxidation of reduced sulfur compounds in a humid environment, *Atmos. Environ.,* 2021, **261**, Art. N0 118504.
29. E. H. Hoffmann, A. Tilgner, R. Schrodner, P. Brauera, R. Wolke, H. Herrmann, An advanced modeling study on the impacts and atmospheric implications of multiphase dimethyl sulfide chemistry, *Proc. Natl. Acad. Sci. USA,* 2016, **113**, 11776-11781.
30. I. Barnes, J. Hjorth, N. Mihalopoulos, Dimethyl sulfide and dimethyl sulfoxide and their oxidation in the atmosphere, *Chem. Rev.,* 2006, **106**, 940-975.
31. R. Wollesen de Jonge, J. Elm, B. Rosati, S. Christiansen, N. Hyttinen, D. Ludemann, M. Bilde, P. Roldin, Secondary aerosol formation from dimethyl sulfide - improved mechanistic understanding based on smog chamber experiments and modelling, *Atmos. Chem. Phys.,* 2021, **21**, 9955–9976.
32. P. R. Veres, J. A. Neuman, T. H. Bertram, E. Assaf, G. M. Wolfe, C. J. Williamson, B. Weinzierl, S. Tilmes, C. R. Thompson, A. B. Thames, J. C. Schroder, A. Saiz-Lopez, A. W. Rollins, J. M. Roberts, D. Price, J. Peischl, B. A. Nault, K. H. Moller, D. O. Miller, S. Meinardi, Q. Y. Li, J. F. Lamarque, A. Kupc, H. G. Kjaergaard, D. Kinnison, J. L. Jimenez, C. M. Jernigan, R. S. Hornbrook, A. Hills, M. Dollner, D. A. Day, C. A. Cuevas, P. Campuzano-Jost, J. Burkholder, T. P. Bui, W. H. Brune, S. S. Brown, C. A. Brock, I. Bourgeois, D. R. Blake, E. C. Apel, T. B. Ryerson, Global airborne sampling reveals a previously unobserved dimethyl sulfide oxidation mechanism in the marine atmosphere, *Proc. Natl. Acad. Sci. USA,* 2020, **117**, 4505-4510.
33. S. F. Watts, The mass budgets of carbonyl sulfide, dimethyl sulfide, carbon disulfide and hydrogen sulfide, *Atmos. Environ.,* 2000, **34**, 761-779.
34. R. J. Charlson, J. E. Lovelock, M. O. Andreae, S. G. Warren, Oceanic phytoplankton, atmospheric sulfur, cloud albedo and climate, *Nature,* 1987, **326**, 655-661.
35. T. S. Bates, B. K. Lamb, A. Guenther, J. Dignon, R. E. Stoiber, Sulfur emissions to the atmosphere from natural sources, *J. Atmos. Chem.,* 1992, **14**, 315-337.
36. A. Lana, T. G. Bell, R. Simo, S. M. Vallina, J. Ballabrera-Poy, A. J. Kettle, J. Dachs, L. Bopp, E. S. Saltzman, J. Stefels, J. E. Johnson, P. S. Liss, An updated climatology of surface dimethlysulfide concentrations and emission fluxes in the global ocean, *Global Biogeochem. Cycles,* 2011, **25**, doi: 10.1029/2010gb003850.
37. M. O. Andreae, P. J. Crutzen, Atmospheric aerosols: Biogeochemical sources and role in atmospheric chemistry, *Science,* 1997, **276**, 1052-1058.
38. V. P. Aneja, Natural sulfur emissions into the atmosphere, *J. Air Waste Manage. Assoc.,* 1990, **40**, 469-476.
39. K. Jardine, A. M. Yanez-Serrano, J. Williams, N. Kunert, A. Jardine, T. Taylor, L. Abrell, P. Artaxo, A. Guenther, C. N. Hewitt, E. House, A. P. Florentino, A. Manzi, N. Higuchi, J. Kesselmeier, T. Behrendt, P. R. Veres, B. Derstroff, J. D. Fuentes, S. T. Martin, M. O. Andreae, Dimethyl sulfide in the Amazon rain forest, *Global Biogeochem. Cycles,* 2015, **29**, 19-32.

40. P. J. Crutzen, J. Williams, U. Poschl, P. Hoor, H. Fischer, C. Warneke, R. Holzinger, A. Hansel, W. Lindinger, B. Scheeren, J. Lelieveld, High spatial and temporal resolution measurements of primary organics and their oxidation products over the tropical forests of Surinam, *Atmos. Environ.,* 2000, **34**, 1161-1165.
41. J. Kesselmeier, F. X. Meixner, U. Hofmann, A. L. Ajavon, S. Leimbach, M. O. Andreae, Reduced sulfur compound exchange between the atmosphere and tropical tree species in Southern Cameroon, *Biogeochemistry,* 1993, **23**, 23-45.
42. S. Meinardi, I. J. Simpson, N. J. Blake, D. R. Blake, F. S. Rowland, Dimethyl disulfide (DMDS) and dimethyl sulfide (DMS) emissions from biomass burning in Australia, *Geosphys. Res. Lett.,* 2003, **30**, Art. N0 1454 (1451-1454).
43. C. E. Stockwell, P. R. Veres, J. Williams, R. J. Yokelson, Characterization of biomass burning emissions from cooking fires, peat, crop residue, and other fuels with high-resolution proton-transfer-reaction time-of-flight mass spectrometry, *Atmos. Chem. Phys.,* 2015, **15**, 845-865.
44. V. Perraud, S. Meinardi, D. R. Blake, B. J. Finlayson-Pitts, Challenges associated with the sampling and analysis of organosulfur compounds in air using real-time PTR-ToF-MS and offline GC-FID, *Atmos. Meas. Tech.,* 2016, **9**, 1325-1340.
45. S. Trabue, K. Scoggin, F. Mitloehner, H. Li, R. Burns, H. Xin, Field sampling method for quantifying volatile sulfur compounds from animal feeding operations, *Atmos. Environ.,* 2008, **42**, 3332-3341.
46. P. Hobbs, T. Mottram, New Directions: Significant contributions of dimethyl sulphide from livestock to the atmosphere, *Atmos. Environ.,* 2000, **34**, 3649-3650.
47. J. S. Vandergheynst, D. J. Cogan, P. J. Defelice, J. M. Gossett, L. P. Walker, Effect of process management on the emission of organosulfur compounds and gaseous antecedents from composting processes, *Environ. Sci. Technol.,* 1998, **32**, 3713-3718.
48. Z. G. Yi, X. M. Wang, G. Y. Sheng, H. M. Fu, Exchange of carbonyl sulfide (OCS) and dimethyl sulfide (DMS) between rice paddy fields and the atmosphere in subtropical China, *Agr Ecosyst Environ,* 2008, **123**, 116-124.
49. P. D. Goldan, W. C. Kuster, D. L. Albritton, F. C. Fehsenfeld, The measurement of natural sulfur emissions from soils and vegetation - 3 Sites in the Eastern-United-States revisited, *J. Atmos. Chem.,* 1987, **5**, 439-467.
50. J. Williams, N. Y. Wang, R. J. Cicerone, K. Yagi, M. Kurihara, F. Terada, Atmospheric methyl halides and dimethyl sulfide from cattle, *Global Biogeochem. Cycles,* 1999, **13**, 485-491.
51. K. C. Li, D. Shooter, Analysis of sulfur-containing compounds in ambient air using solid-phase microextraction and gas chromatography with pulsed flame photometric detection, *Int. J. Environ. Anal. Chem.,* 2004, **84**, 749-760.
52. M. R. Ras, F. Borrull, R. M. Marce, Determination of volatile organic sulfur compounds in the air at sewage management areas by thermal desorption and gas chromatography-mass spectrometry, *Talanta,* 2008, **74**, 562-569.
53. E. Smet, H. Van Langenhove, Abatement of volatile organic sulfur compounds in odorous emissions from the bio-industry, *Biodegradation,* 1998, **9**, 273-284.
54. R. Raiswell, S. H. Bottrel, The disposal of flue gas desulphurisation waste: sulphur gas emissions and their control, *Environ. Geochem. Health,* 1991, **13**, 119-126.

55. P. R. Mulay, P. Cavicchia, S. M. Watkins, A. Tovar-Aguilar, M. Wiese, G. M. Calvert, Acute illness associated with exposure to a new soil fumigant containing dimethyl disulfide - Hillsborough County, Florida, 2014, *J Agromedicine,* 2016, **21**, 373-379.
56. D. D. Yan, A. C. Cao, Q. X. Wang, Y. Li, C. B. Ouyang, M. X. Guo, X. Q. Guo, Dimethyl disulfide (DMDS) as an effective soil fumigant against nematodes in China, *Plos One,* 2019, **14**.
57. J. Fritsch, T. Fouillet, P. Charles, P. Fargier-Puech, C. Ramponi-Bur, S. Descamps, G. Du Fretay, A. Myrta, French experiences with dimethyl disulfide (DMDS) as a nematicide in vegetable crops, *Acta Hortic,* 2014, **1044**, 427-433.
58. F. L. Suarez, J. K. Furne, J. Springfield, M. D. Levitt, Morning breath odor: Influence of treatments on sulfur gases, *J. Dent. Res.,* 2000, **79**, 1773-1777.
59. S. Meinardi, K. B. Jin, B. Barletta, D. R. Blake, N. D. Vaziri, Exhaled breath and fecal volatile organic biomarkers of chronic kidney disease, *Biochim. Biophys. Acta, Gen. Subj.,* 2013, **1830**, 2531-2537.
60. H. Berresheim, M. Adam, C. Monahan, C. O'Dowd, J. M. C. Plane, B. Bohn, F. Rohrer, Missing SO_2 oxidant in the coastal atmosphere? - Observations from high-resolution measurements of OH and atmospheric sulfur compounds, *Atmos. Chem. Phys.,* 2014, **14**, 12209-12223.
61. H. Berresheim, T. Elste, H. G. Tremmel, A. G. Allen, H. C. Hansson, K. Rosman, M. Dal Maso, J. M. Makela, M. Kulmala, C. D. O'Dowd, Gas-aerosol relationships of H_2SO_4, MSA, and OH: Observations in the coastal marine boundary layer at Mace Head, Ireland, *J. Geophys. Res.,* 2002, **107**, Art N0 D19, 8100 (PAR 8105-8101 - PAR 8105-8112).
62. F. L. Eisele, D. J. Tanner, Measurement of the gas-phase concentration of H_2SO_4 and methane sulfonic acid and estimates of H_2SO_4 production and loss in the atmosphere., *J. Geophys. Res.,* 1993, **98**, 9001-9010.
63. A. Jefferson, D. J. Tanner, F. L. Eisele, D. D. Davis, G. Chen, J. Crawford, J. W. Huey, A. L. Torres, H. Berresheim, OH photochemistry and methane sulfonic acid formation in the coastal Antarctic boundary layer, *J. Geophys. Res.,* 1998, **103**, 1647-1656.
64. C. D. O'Dowd, K. Hameri, J. M. Makela, L. Pirjola, M. Kulmala, S. G. Jennings, H. Berresheim, H. C. Hansson, G. de Leeuw, G. J. Kunz, A. G. Allen, C. N. Hewitt, A. Jackson, Y. Viisanen, T. Hoffmann, A dedicated study of New Particle Formation and Fate in the Coastal Environment (PARFORCE): Overview of objectives and achievements, *J. Geophys. Res.,* 2002, **107**, Art No 8108.
65. H. Bardouki, H. Berresheim, M. Vrekoussis, J. Sciare, G. Kouvarakis, K. Oikonomou, J. Schneider, N. Mihalopoulos, Gaseous (DMS, MSA, SO_2, H_2SO_4 and DMSO) and particulate (sulfate and methanesulfonate) sulfur species over the northeastern coast of Crete, *Atmos. Chem. Phys.,* 2003, **3**, 1871-1886.
66. L. J. Beck, N. Sarnela, H. Junninen, C. J. M. Hoppe, O. Garmash, F. Bianchi, M. Riva, C. Rose, O. Perakyla, D. Wimmer, O. Kausiala, T. Jokinen, L. Ahonen, J. Mikkila, J. Hakala, X. C. He, J. Kontkanen, K. K. E. Wolf, D. Cappelletti, M. Mazzola, R. Traversi, C. Petroselli, A. P. Viola, V. Vitale, R. Lange, A. Massling, J. K. Nojgaard, R. Krejci, L. Karlsson, P. Zieger, S. Jang, K. Lee, V. Vakkari, J. Lampilahti, R. C. Thakur, K. Leino, J. Kangasluoma, E. M. Duplissy, E. Siivola, M. Marbouti, Y. J. Tham, A. Saiz-Lopez, T. Petaja, M. Ehn, D. R. Worsnop, H. Skov, M. Kulmala, V. M. Kerminen, M. Sipila,

Differing mechanisms of new particle formation at two Arctic sites, *Geosphys. Res. Lett.,* 2021, **48**, Art. No e2020GL091334.

67. M. J. Lawler, M. P. Rissanen, M. Ehn, R. L. Mauldin, N. Sarnela, M. Sipilä, J. N. Smith, Evidence for diverse biogeochemical drivers of boreal forest new particle formation, *Geosphys. Res. Lett.,* 2018, **45**, 2038-2046.

68. R. L. Mauldin, C. A. Cantrell, M. Zondlo, E. Kosciuch, F. L. Eisele, G. Chen, D. Davis, R. Weber, J. Crawford, D. Blake, A. Bandy, D. Thornton, Highlights of OH, H_2SO_4, and methane sulfonic acid measurements made aboard the NASA P-3B during Transport and Chemical Evolution over the Pacific, *J. Geophys. Res.,* 2003, **108**, Art. No 8796.

69. L. L. J. Quelever, L. Dada, E. Asmi, J. Lampilahti, T. Chan, J. E. Ferrara, G. E. Copes, G. Perez-Fogwill, L. Barreira, M. Aurela, D. R. Worsnop, T. Jokinen, M. Sipila, Investigation of new particle formation mechanisms and aerosol processes at Marambio Station, Antarctic Peninsula, *Atmos. Chem. Phys.,* 2022, **22**, 8417-8437.

70. D. Davis, G. Chen, P. Kasibhatla, A. Jefferson, D. Tanner, F. Eisele, D. Lenschow, W. Neff, H. Berresheim, DMS oxidation in the Antarctic marine boundary layer: Comparison of model simulations and field observations of DMS, DMSO, $DMSO_2$, H_2SO_4(g), MSA(g), and MSA(p), *J. Geophys. Res.,* 1998, **103**, 1657-1678.

71. E. S. Saltzman, D. L. Savoie, R. G. Zika, J. M. Prospero, Methane sulfonic acid in the marine atmosphere, *J. Geophys. Res-Oceans,* 1983, **88**, 897-902.

72. S. Huang, L. Poulain, D. van Pinxteren, M. van Pinxteren, Z. J. Wu, H. Herrmann, A. Wiedensohler, Latitudinal and seasonal distribution of particulate MSA over the Atlantic using a validated quantification method with HR-ToF-AMS, *Environ. Sci. Technol.,* 2017, **51**, 418-426.

73. L. Phinney, W. R. Leaitch, U. Lohmann, H. Boudries, D. R. Worsnop, J. T. Jayne, D. Toom-Sauntry, M. Wadleigh, S. Sharma, N. Shantz, Characterization of the aerosol over the sub-arctic north east Pacific Ocean, *Deep-Sea Res Pt II,* 2006, **53**, 2410-2433.

74. A. Sorooshian, L. T. Padro, A. Nenes, G. Feingold, A. McComiskey, S. P. Hersey, H. Gates, H. H. Jonsson, S. D. Miller, G. L. Stephens, R. C. Flagan, J. H. Seinfeld, On the link between ocean biota emissions, aerosol, and maritime clouds: Airborne, ground, and satellite measurements off the coast of California, *Global Biogeochem. Cycles,* 2009, **23**, 1-15.

75. D. D. Huang, Y. J. Li, B. P. Lee, C. K. Chan, Analysis of organic sulfur compounds in atmospheric aerosols at the HKUST supersite in Hong Kong using HR-ToF-AMS, *Environ. Sci. Technol.,* 2015, **49**, 3672-3679.

76. M. D. Willis, J. Burkart, J. L. Thomas, F. Kollner, J. Schneider, H. Bozem, P. M. Hoor, A. A. Aliabadi, H. Schulz, A. B. Herber, W. R. Leaitch, J. P. D. Abbatt, Growth of nucleation mode particles in the summertime Arctic: a case study, *Atmos. Chem. Phys.,* 2016, **16**, 7663-7679.

77. L. C. Maudlin, Z. Wang, H. H. Jonsson, A. Sorooshian, Impact of wildfires on size-resolved aerosol composition at a coastal California site, *Atmos. Environ.,* 2015, **119**, 59-68.

78. A. Sorooshian, E. Crosbie, L. C. Maudlin, J. S. Youn, Z. Wang, T. Shingler, A. M. Ortega, S. Hersey, R. K. Woods, Surface and airborne measurements of organosulfur and

methanesulfonate over the western United States and coastal areas, *J. Geophys. Res.,* 2015, **120**, 8535-8548.
79. C. Stahl, M. T. Cruz, P. A. Banaga, G. Betito, R. A. Braun, M. A. Aghdam, M. O. Cambaliza, G. R. Lorenzo, A. B. MacDonald, M. R. A. Hilario, P. C. Pabroa, J. R. Yee, J. B. Simpas, A. Sorooshian, Sources and characteristics of size-resolved particulate organic acids and methanesulfonate in a coastal megacity: Manila, Philippines, *Atmos. Chem. Phys.,* 2020, **20**, 15907-15935.
80. C. J. Gaston, K. A. Pratt, X. Y. Qin, K. A. Prather, Real-time detection and mixing state of methanesulfonate in single particles at an inland urban location during a phytoplankton bloom, *Environ. Sci. Technol.,* 2010, **44**, 1566-1572.
81. H. Yuan, Y. Wang, G. S. Zhuang, MSA in Beijing aerosol, *Chin. Sci. Bull.,* 2004, **49**, 1020-1025.
82. V. M. Kerminen, M. Aurela, R. E. Hillamo, A. Virkkula, Formation of particulate MSA: Deductions from size distribution measurements in the Finnish Arctic, *Tellus B,* 1997, **49**, 159-171.
83. M. J. Lawler, E. S. Saltzman, L. Karlsson, P. Zieger, M. Salter, A. Baccarini, J. Schmale, C. Leck, New insights into the composition and origins of ultrafine aerosol in the summertime high Arctic, *Geosphys. Res. Lett.,* 2021, **48**, Art No e2021GL094395.
84. J. Burkart, M. D. Willis, H. Bozem, J. L. Thomas, K. Law, P. Hoor, A. A. Aliabadi, F. Kollner, J. Schneider, A. B. Herber, J. D. Abbatt, W. R. Leaitch, Summertime observations of elevated levels of ultrafine particles in the high Arctic marine boundary layer, *Atmos. Chem. Phys.,* 2017, **17**, 5515-5535.
85. K. T. Park, S. Jang, K. Lee, Y. J. Yoon, M. S. Kim, K. Park, H. J. Cho, J. H. Kang, R. Udisti, B. Y. Lee, K. H. Shin, Observational evidence for the formation of DMS-derived aerosols during Arctic phytoplankton blooms, *Atmos. Chem. Phys.,* 2017, **17**, 9665-9675.
86. X. X. Li, Y. Y. Li, M. J. Lawler, J. M. Hao, J. N. Smith, J. K. Jiang, Composition of ultrafine particles in urban Beijing: Measurement using a thermal desorption chemical ionization mass spectrometer, *Environ. Sci. Technol.,* 2021, **55**, 2859-2868.
87. T. A. Pakkanen, V. M. Kerminen, C. H. Korhonen, R. E. Hillamo, P. Aarnio, T. Koskentalo, W. Maenhaut, Urban and rural ultrafine (PM(0.1)) particles in the Helsinki area, *Atmos. Environ.,* 2001, **35**, 4593-4607.
88. K. N. Fossum, J. Ovadnevaite, D. Ceburnis, M. Dall'Osto, S. Marullo, M. Bellacicco, R. Simo, D. T. Liu, M. Flynn, A. Zuend, C. O'Dowd, Summertime primary and secondary contributions to Southern ocean cloud condensation nuclei, *Sci. Rep.,* 2018, **8**, Art No 13844.
89. J. M. Makela, S. Yli-Koivisto, V. Hiltunen, W. Seidl, E. Swietlicki, K. Teinila, M. Sillanpaa, I. K. Koponen, J. Paatero, K. Rosman, K. Hameri, Chemical composition of aerosol during particle formation events in boreal forest, *Tellus B,* 2001, **53**, 380-393.
90. M. Dall'Osto, D. C. S. Beddows, P. Tunved, R. Krejci, J. Strom, H. C. Hansson, Y. J. Yoon, K. T. Park, S. Becagli, R. Udisti, T. Onasch, C. D. O'Dowd, R. Simo, R. M. Harrison, Arctic sea ice melt leads to atmospheric new particle formation, *Sci. Rep.,* 2017, **7**, 1-10.

91. P. K. Quinn, T. L. Miller, T. S. Bates, J. A. Ogren, E. Andrews, G. E. Shaw, A 3-year record of simultaneously measured aerosol chemical and optical properties at Barrow, Alaska, *J. Geophys. Res.,* 2002, **107**, Art No. 4130.
92. W. R. Leaitch, S. Sharma, L. Huang, D. Toom-Sauntry, A. Chivulescu, A.-M. Macdonald, K. von Salzen, J. R. Pierce, A. K. Bertram, J. C. Schroder, N. C. Shantz, R. Y.-W. Chang, A.-L. Norman, Dimethyl sulfide control of the clean summertime Arctic aerosol and cloud, *Elementa Sci. Anthrop.,* 2013, **1**, 1-12.
93. M. Dall'Osto, R. Simo, R. M. Harrison, D. C. S. Beddows, A. Saiz-Lopez, R. Lange, H. Skov, J. K. Nojgaard, I. E. Nielsen, A. Massling, Abiotic and biotic sources influencing spring new particle formation in North East Greenland, *Atmos. Environ.,* 2018, **190**, 126-134.
94. M. D. Willis, W. R. Leaitch, J. P. D. Abbatt, Processes controlling the composition and abundance of Arctic aerosol, *Rev. Geophys.,* 2018, **56**, 621-671.
95. Q. Chen, T. Sherwen, M. Evans, B. Alexander, DMS oxidation and sulfur aerosol formation in the marine troposphere: a focus on reactive halogen and multiphase chemistry, *Atmos. Chem. Phys.,* 2018, **18**, 13617-13637.
96. M. Gali, E. Devred, M. Babin, M. Levasseur, Decadal increase in Arctic dimethylsulfide emission, *Proc. Natl. Acad. Sci. USA,* 2019, **116**, 19311-19317.
97. S. Sharma, E. Chan, M. Ishizawa, D. Toom-Sauntry, S. L. Gong, S. M. Li, D. W. Tarasick, W. R. Leaitch, A. Norman, P. K. Quinn, T. S. Bates, M. Levasseur, L. A. Barrie, W. Maenhaut, Influence of transport and ocean ice extent on biogenic aerosol sulfur in the Arctic atmosphere, *J. Geophys. Res.,* 2012, **117**, Art No. D12209.
98. S. Becagli, L. Lazzara, C. Marchese, U. Dayan, S. E. Ascanius, M. Cacciani, L. Caiazzo, C. Di Biagio, T. Di Iorio, A. di Sarra, P. Eriksen, F. Fani, F. Giardi, D. Meloni, G. Muscari, G. Pace, M. Severi, R. Traversi, R. Udisti, Relationships linking primary production, sea ice melting, and biogenic aerosol in the Arctic, *Atmos. Environ.,* 2016, **136**, 1-15.
99. K. D. Arquero, R. B. Gerber, B. J. Finlayson-Pitts, The role of oxalic acid in new particle formation from methanesulfonic acid, methylamine, and water, *Environ. Sci. Technol.,* 2017, **51**, 2124-2130.
100. K. D. Arquero, J. Xu, R. B. Gerber, B. J. Finlayson-Pitts, Particle formation and growth from oxalic acid, methanesulfonic acid, trimethylamine and water: a combined experimental and theoretical study, *Phys. Chem. Chem. Phys.,* 2017, **19**, 28286-28301.
101. H. Chen, M. J. Ezell, K. D. Arquero, M. E. Varner, M. L. Dawson, R. B. Gerber, B. J. Finlayson-Pitts, New particle formation and growth from methanesulfonic acid, trimethylamine and water, *Phys. Chem. Chem. Phys.,* 2015, **17**, 13699-13709.
102. H. Chen, M. E. Varner, R. B. Gerber, B. J. Finlayson-Pitts, Reactions of methanesulfonic acid with amines and ammonia as a source of new particles in air, *J. Phys. Chem. B,* 2016, **120**, 1526-1536.
103. H. H. Chen, B. J. Finlayson-Pitts, New particle formation from methanesulfonic acid and amines/ammonia as a function of temperature, *Environ. Sci. Technol.,* 2017, **51**, 243-252.
104. M. L. Dawson, M. E. Varner, V. Perraud, M. J. Ezell, R. B. Gerber, B. J. Finlayson-Pitts, Simplified mechanism for new particle formation from methanesulfonic acid, amines,

and water via experiments and ab initio calculations, *Proc. Natl. Acad. Sci. USA,* 2012, **109**, 18719-18724.
105. V. Perraud, X. X. Li, J. K. Jiang, B. J. Finlayson-Pitts, J. N. Smith, Size-resolved chemical composition of sub-20 nm particles from methanesulfonic acid reactions with methylamine and ammonia, *ACS Earth Space Chem.,* 2020, **4**, 1182-1194.
106. V. Perraud, J. Xu, R. B. Gerber, B. J. Finlayson-Pitts, Integrated experimental and theoretical approach to probe the synergistic effect of ammonia in methanesulfonic acid reactions with small alkylamines, *Environ. Sci. Processes Impacts,* 2020, **22**, 305-328.
107. J. S. Johnson, C. N. Jen, Role of methanesulfonic acid in sulfuric acid-amine and ammonia new particle formation, *ACS Earth Space Chem.,* 2023, **7**, 653-660.
108. J. Shen, H.-B. Xie, J. Elm, F. Ma, J. Chen, H. Vehkamaki, Methanesulfonic acid-driven new particle formation enhanced by monoethanolamine: A computational study, *Environ. Sci. Technol.,* 2019, **53**, 14387-14397.
109. J. W. Shen, J. Elm, H. B. Xie, J. W. Chen, J. F. Niu, H. Vehkamaki, Structural effects of amines in enhancing methanesulfonic acid-driven new particle formation, *Environ. Sci. Technol.,* 2020, **54**, 13498-13508.
110. H. L. Zhao, X. T. Jiang, L. Du, Contribution of methane sulfonic acid to new particle formation in the atmosphere, *Chemosphere,* 2017, **174**, 689-699.
111. F. R. Rasmussen, J. Kubecka, J. Elm, Contribution of methansulfonic acid to the formation of molecular clusters in the marine atmosphere, *J. Phys. Chem. A,* 2022, **126**, 7127-7136.
112. J. Elm, Clusteromics II: Methansulfonic acid-base cluster formation, *ACS Omega,* 2021, **6**, 17035-17044.
113. R. Zhang, J. Shen, H.-B. Xie, J. Chen, J. Elm, The role of organic acids in new particle formation from methanesulfonic acid and methylamine, *Atmos. Chem. Phys.,* 2022, **22**, 2639-2650.
114. S. Chee, K. Barsanti, J. N. Smith, N. Myllys, A predictive model for salt nanoparticle formation using heterodimer stability calculations, *Atmos. Chem. Phys.,* 2021, **21**, 11637-11654.
115. D. P. Chen, D. F. Li, C. W. Wang, F. Y. Liu, W. L. Wang, Formation mechanism of methanesulfonic acid and ammonia clusters: A kinetics simulation study, *Atmos. Environ.,* 2020, **222**.
116. M. van Pinxteren, B. Fiedler, D. van Pinxteren, Y. Iinuma, A. Kortzinger, H. Herrmann, Chemical characterization of sub-micrometer aerosol particles in the tropical Atlantic Ocean: marine and biomass burning influences, *J. Atmos. Chem.,* 2015, **72**, 105-125.
117. C. Muller, Y. Iinuma, J. Karstensen, D. van Pinxteren, S. Lehmann, T. Gnauk, H. Herrmann, Seasonal variation of aliphatic amines in marine sub-micrometer particles at the Cape Verde islands, *Atmos. Chem. Phys.,* 2009, **9**, 9587-9597.
118. M. C. Facchini, S. Decesari, M. Rinaldi, C. Carbone, E. Finessi, M. Mircea, S. Fuzzi, F. Moretti, E. Tagliavini, D. Ceburnis, C. D. O'Dowd, Important source of marine secondary organic aerosol from biogenic amines, *Environ. Sci. Technol.,* 2008, **42**, 9116-9121.

119. X. F. Huang, C. R. Deng, G. S. Zhuang, J. Lin, M. X. Xiao, Quantitative analysis of aliphatic amines in urban aerosols based on online derivatization and high performance liquid chromatography, *Environ Sci-Proc Imp,* 2016, **18**, 796-801.
120. H. Feng, X. N. Ye, Y. X. Liu, Z. K. Wang, T. X. Gao, A. Y. Cheng, X. F. Wang, J. M. Chen, Simultaneous determination of nine atmospheric amines and six inorganic ions by non-suppressed ion chromatography using acetonitrile and 18-crown-6 as eluent additive, *J. Chromatogr. A,* 2020, **1624**, Art No 461234.
121. M. Wang, Q. Y. Wang, S. S. H. Ho, H. Li, R. J. Zhang, W. K. Ran, L. L. Qu, S. C. Lee, J. J. Cao, Chemical characteristics and sources of nitrogen-containing organic compounds at a regional site in the North China Plain during the transition period of autumn and winter, *Sci. Total Environ.,* 2022, **812**, Art No 151451.
122. A. P. Sullivan, K. B. Benedict, C. M. Carrico, M. K. Dubey, B. A. Schichtel, J. C. Collett, A quantitative method to measure and speciate amines in ambient aerosol samples, *Atmosphere,* 2020, **11**, ART No 808.
123. Q. Zhang, C. Anastasio, Free and combined amino compounds in atmospheric fine particles (PM2.5) and fog waters from Northern California, *Atmos. Environ.,* 2003, **37**, 2247-2258.
124. Z. Y. Liu, M. Li, X. F. Wang, Y. H. Liang, Y. R. Jiang, J. Chen, J. S. Mu, Y. J. Zhu, H. Meng, L. X. Yang, K. Y. Hou, Y. F. Wang, L. K. Xue, Large contributions of anthropogenic sources to amines in fine particles at a coastal area in northern China in winter, *Sci. Total Environ.,* 2022, **839**, ARTN 156281.
125. B. K. Place, A. T. Quilty, R. A. Di Lorenzo, S. E. Ziegler, T. C. VandenBoer, Quantitation of 11 alkylamines in atmospheric samples: separating structural isomers by ion chromatography, *Atmos. Meas. Tech.,* 2017, **10**, 1061-1078.
126. K. Gorzelska, J. N. Galloway, Amine nitrogen in the atmospheric environment over the north Atlantic ocean, *Global Biogeochem. Cycles,* 1990, **4**, 309-333.
127. V. M. Kerminen, X. Chen, V. Vakkari, T. Petaja, M. Kulmala, F. Bianchi, Atmospheric new particle formation and growth: review of field observations, *Environ. Res. Lett.,* 2018, **13**, Art No 103003 (103001-103038 p).
128. U. Poschl, Atmospheric aerosols: Composition, transformation, climate and health effects, *Angew Chem Int Edit,* 2005, **44**, 7520-7540.
129. IPCC (2021) Climate Change 2021: The Physical Science Basis. Contribution of Working Group I to the Sixth Assessment Report of the Intergovernmental Panel on Climate Change. eds V. Masson-Delmotte *et al.* (United Kindom and New York, NY, USA), p 2391 pp.
130. A. L. Hodshire, P. Campuzano-Jost, J. K. Kodros, B. Croft, B. A. Nault, J. C. Schroder, J. L. Jimenez, J. R. Pierce, The potential role of methanesulfonic acid (MSA) in aerosol formation and growth and the associated radiative forcings, *Atmos. Chem. Phys.,* 2019, **19**, 3137-3160.
131. C. A. Pope, D. W. Dockery, Health effects of fine particulate air pollution: Lines that connect, *J. Air Waste Manage. Assoc.,* 2006, **56**, 709-742.
132. M. R. Heal, P. Kumar, R. M. Harrison, Particles, air quality, policy and health, *Chem. Soc. Rev.,* 2012, **41**, 6606-6630.
133. J. Lelieveld, Clean air in the Anthropocene, *Faraday Discuss.,* 2017, **200**, 693-703.

134. J. Lelieveld, J. S. Evans, M. Fnais, D. Giannadaki, A. Pozzer, The contribution of outdoor air pollution sources to premature mortality on a global scale, *Nature,* 2015, **525**, 367-+.
135. A. L. Moreno-Ríos, L. P. Tejeda-Benítez, C. F. Bustillo-Lecompte, Sources, characteristics, toxicity, and control of ultrafine particles: An overview, *Geosci Front,* 2022, **13**.
136. S. W. Sang, C. Chu, T. C. Zhang, H. Chen, X. R. Yang, The global burden of disease attributable to ambient fine particulate matter in 204 countries and territories, 1990-2019: A systematic analysis of the Global Burden of Disease Study 2019, *Ecotox. Environ. Safe.,* 2022, **238**, Art. N0 113588 (113581-113511).
137. X. J. Deng, X. X. Tie, D. Wu, X. J. Zhou, X. Y. Bi, H. B. Tan, F. Li, C. L. Hang, Long-term trend of visibility and its characterizations in the Pearl River Delta (PRD) region, China, *Atmos. Environ.,* 2008, **42**, 1424-1435.
138. D. Chang, Y. Song, B. Liu, Visibility trends in six megacities in China 1973-2007, *Atmos. Res.,* 2009, **94**, 161-167.
139. A. Singh, W. J. Bloss, F. D. Pope, 60 years of UK visibility measurements: impact of meteorology and atmospheric pollutants on visibility, *Atmos. Chem. Phys.,* 2017, **17**, 2085-2101.
140. J. G. Watson, Visibility: science and regulation, *J. Air Waste Manage. Assoc.,* 2002, **52**, 628-713.
141. A. L. Moreno-Rios, L. P. Tejeda-Benitez, C. F. Bustillo-Lecompte, Sources, characteristics, toxicity, and control of ultrafine particles: An overview, *Geosci Front,* 2022, **13**, Art No 101147.
142. M. J. Ezell, H. Chen, K. D. Arquero, B. J. Finlayson-Pitts, Aerosol fast flow reactor for laboratory studies of new particle formation, *J. Aerosol Sci.,* 2014, **78**, 30-40.
143. J. N. Smith, K. F. Moore, P. H. McMurry, F. L. Eisele, Atmospheric measurements of sub-20 nm diameter particle chemical composition by thermal desorption chemical ionization mass spectrometry, *Aerosol Sci. Technol.,* 2004, **38**, 100-110.
144. D. Voisin, J. N. Smith, H. Sakurai, P. H. McMurry, F. L. Eisele, Thermal desorption chemical ionization mass spectrometer for ultrafine particle chemical composition, *Aerosol Sci. Technol.,* 2003, **37**, 471-475.
145. M. J. Lawler, P. M. Winkler, J. Kim, L. Ahlm, J. Trostl, A. P. Praplan, S. Schobesberger, A. Kuerten, J. Kirkby, F. Bianchi, J. Duplissy, A. Hansel, T. Jokinen, H. Keskinen, K. Lehtipalo, M. Leiminger, T. Petaja, M. Rissanen, L. Rondo, M. Simon, M. Sipila, C. Williamson, D. Wimmer, I. Riipinen, A. Virtanen, J. N. Smith, Unexpectedly acidic nanoparticles formed in dimethylamine-ammonia-sulfuric-acid nucleation experiments at CLOUD, *Atmos. Chem. Phys.,* 2016, **16**, 13601-13618.
146. H. Chen, S. Chee, M. J. Lawler, K. C. Barsanti, B. M. Wong, J. N. Smith, Size resolved chemical composition of nanoparticles from reactions of sulfuric acid with ammonia and dimethylamine, *Aerosol Sci. Technol.,* 2018, **52**, 1120-1133.
147. D.-R. Chen, D. Y. Pui, A high efficiency, high throughput unipolar aerosol charger for nanoparticles, *J. Nanopart. Res.,* 1999, **1**, 115-126.

148. P. H. McMurry, A. Ghimire, H.-K. Ahn, H. Sakurai, K. Moore, M. Stolzenburg, J. N. Smith, Sampling nanoparticles for chemical analysis by low resolution electrical mobility classification, *Environ. Sci. Technol.,* 2009, **43**, 4653-4658.
149. D. V. Davis, R. G. Cooks, Site of protonation and bifunctional group-interactions in a,w-hydroxyalkylamines, *Org. Mass Spectrom.,* 1981, **16**, 176-179.
150. G. Bouchoux, N. Choret, F. Berruyer-Penaud, R. Flammang, Thermochemistry and unimolecular reactivity of protonated alpha,omega-aminoalcohols in the gas phase, *Int. J. Mass Spectrom.,* 2002, **217**, 195-230.
151. E. P. L. Hunter, S. G. Lias, Evaluated gas phase basicities and proton affinities of molecules: An update, *J. Phys. Chem. Ref. Data,* 1998, **27**, 413-656.
152. S. Kapteina, K. Slowik, S. P. Verevkin, A. Heintz, Vapor pressures and vaporization enthalpies of a series of ethanolamines, *J. Chem. Eng. Data,* 2005, **50**, 398-402.
153. I. N. Tang, H. R. Munkelwitz, Determination of vapor-pressure from droplet evaporation kinetics, *J. Colloid Interface Sci.,* 1991, **141**, 109-118.
154. S.-L. von der Weiden, F. Drewnick, S. Borrmann, Particle loss calculator - A new software tool for the assessment of the performace of aerosol inlet systems, *Atmos. Meas. Tech.,* 2009, **2**, 469-494.
155. M. Kulmala, H. Vehkamäki, T. Petäjä, M. Dal Maso, A. Lauri, V. M. Kerminen, W. Birmili, P. H. McMurry, Formation and growth rates of ultrafine atmospheric particles: a review of observations, *J. Aerosol Sci.,* 2004, **35**, 143-176.
156. T. L. Greaves, A. Weerawardena, C. Fong, I. Krodkiewska, C. J. Drummond, Protic ionic liquids: Solvents with tunable phase behavior and physicoschemical properties, *J. Phys. Chem. B,* 2006, **110**, 22479-22487.
157. G. Cai, S. Yang, Q. Zhou, L. Liu, J. Xu, S. Zhang, Physicochemical properties of various 2-hydroxyethylammonium sulfonate-based protic ionic liquids and their potential application in hydrodeoxygenation, *Frontiers in Chemistry,* 2019, **7**, art. No 196 (191-112).
158. X. Lu, J. M. Vincent-Luna, S. Calero, M. Roldan-Ruiz, R. Jimenez, M. L. Ferrer, M. C. Gutierrez, F. del Monte, Aqueous co-solvent in zwitterionic-based protic ionic liquids as electrolytes in 2.0 V supercapacitors, *ChemSusChem,* 2020, **13**, 5983-5995.
159. S. J. Brown, D. Yalcin, S. Pnadiancherri, T. C. Le, I. O'rhan, K. Hearn, Q. Han, C. J. Drummond, T. L. Greaves, Characterising a protic ionic liquid library with applied machine learning algorithms, *J. Mol. Liq.,* 2022, **367**, Art No 120453 (120451-120417).
160. R. McGraw, A. Laaksonen, Scaling properties of the critical nucleus in classical and molecular-based theories of vapor-liquid nucleation, *Phys. Rev. Lett.,* 1996, **76**, 2754-2757.
161. O. Kupiainen-Maatta, T. Olenius, H. Korhonen, J. Malilal, M. Dal Maso, K. Lehtinen, H. Vehkamaki, Critical cluster size cannot in pracctice be determined by slope analysis in atmospherically relevant applications, *J. Aerosol Sci.,* 2014, **77**, 127-144.
162. Y. Liu, H. B. Xie, F. F. Ma, J. W. Chen, J. Elm, Amine-enhanced methanesulfonic acid driven nucleation: Predictive model and cluster formation mechanism, *Environ. Sci. Technol.,* 2022, **56**, 7751-7760.

163. J. Xu, V. Perraud, B. J. Finlayson-Pitts, R. B. Gerber, Uptake of water by an acid-base nanoparticle: theoretical and experimental studies of the methanesulfonic acid-methylamine system, *Phys. Chem. Chem. Phys.,* 2018, **20**, 22249-22259.
164. V. Perraud, J. R. Horne, A. S. Martinez, J. Kalinowski, S. Meinardi, M. L. Dawson, L. M. Wingen, D. Dabdub, D. R. Blake, R. B. Gerber, B. J. Finlayson-Pitts, The future of airborne sulfur-containing particles in the absence of fossil fuel sulfur dioxide emissions, *Proc. Natl. Acad. Sci. USA,* 2015, **112**, 13514-13519.
165. J. G. Murphy, P. K. Gregoire, A. G. Tevlin, G. R. Wentworth, R. A. Ellis, M. Z. Markovic, T. C. VandenBoer, Observational constraints on particle acidity using measurements and modelling of particles and gases, *Faraday Discuss.,* 2017, **200**, 379-395.
166. Z. Klimont, S. J. Smith, J. Cofala, The last decade of global anthropogenic sulfur dioxide: 2000-2011 emissions, *Environ. Res. Lett.,* 2013, **8**, 1-6.
167. T. J. Breider, L. J. Mickley, D. J. Jacob, C. Ge, J. Wang, M. P. Sulprizio, B. Croft, D. A. Ridley, J. R. McConnell, S. Sharma, L. Husain, V. A. Dutkiewicz, K. Eleftheriadis, H. Skov, P. K. Hopke, Multidecadal trends in aerosol radiative forcing over the Arctic: Contribution of changes in anthropogenic aerosol to Arctic warming since 1980, *J. Geophys. Res.,* 2017, **122**, 3573-3594.
168. G. M. Hidy, C. L. Blanchard, The changing face of lower tropospheric sulfur oxides in the United States, *Elementa-Sci. Anthrop.,* 2016, **4**, Art. N0 000138 (000131-000120).
169. D. I. Stern, Global sulfur emissions from 1850 to 2000, *Chemosphere,* 2005, **58**, 163-175.
170. M. Amann, Z. Klimont, F. Wagner, Regional and global emissions of air pollutants: Recent trends and future scenarios, *Ann. Rev. Environ. Resour.,* 2013, **38**, 31-55.
171. P. K. Quinn, G. Shaw, E. Andrews, E. G. Dutton, T. Ruoho-Airola, S. L. Gong, Arctic haze: current trends and knowledge gaps, *Tellus B,* 2007, **59**, 99-114.
172. D. Hirdman, J. F. Burkhart, H. Sodemann, S. Eckhardt, A. Jefferson, P. K. Quinn, S. Sharma, J. Strom, A. Stohl, Long-term trends of black carbon and sulphate aerosol in the Arctic: changes in atmospheric transport and source region emissions, *Atmos. Chem. Phys.,* 2010, **10**, 9351-9368.

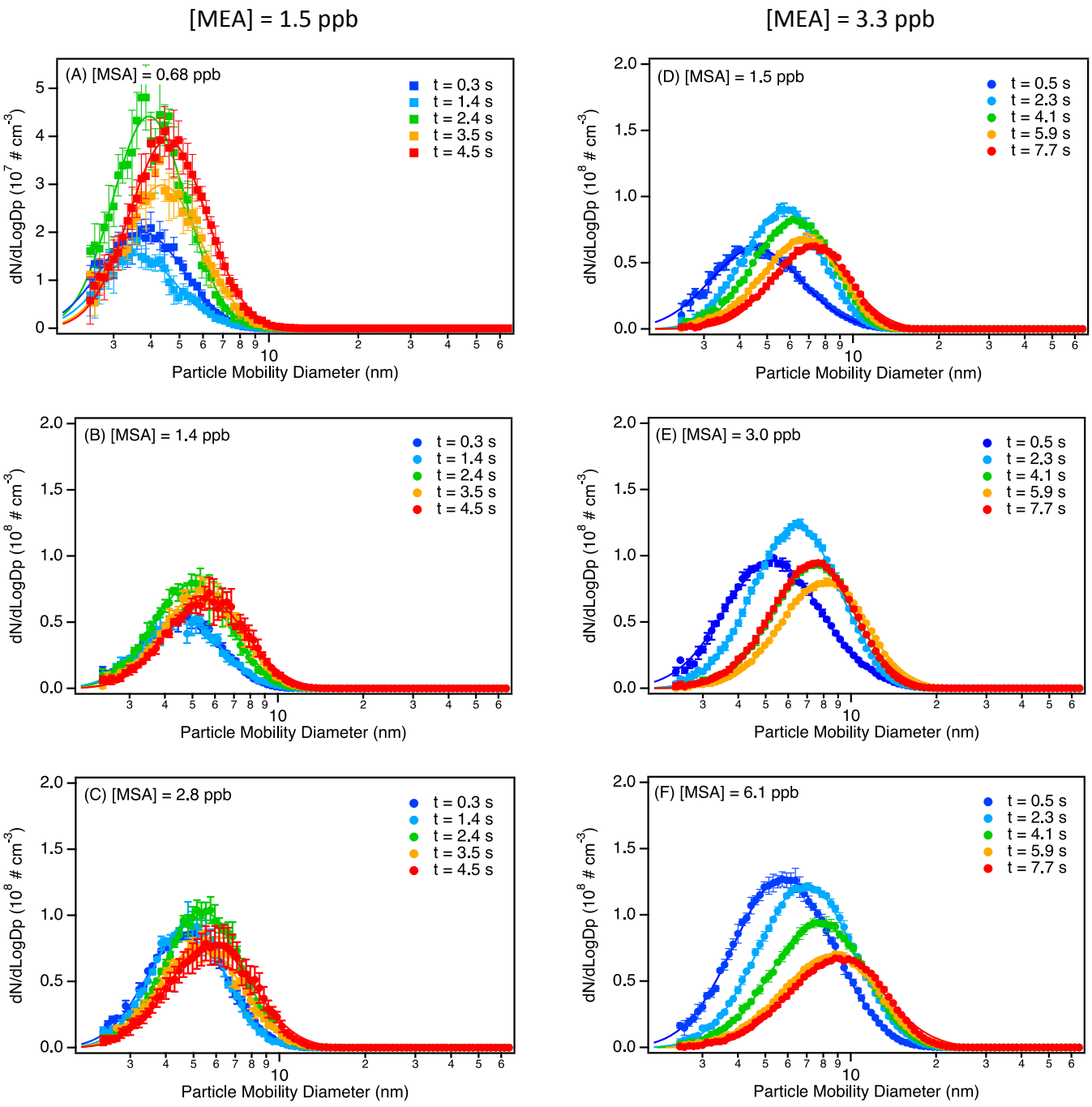

Figure 1. Size distributions of particles from MEA (1.5 ppb) reacting with (A) 0.68 ppb MSA, (B) 1.4 ppb MSA and (C) 2.8 ppb MSA, and size distribution from MEA (3.3 ppb) reacting with (D) 1.5 ppb MSA, (E) 3.3 ppb MSA and (F) 6.1 ppb MSA. Measurements were conducted at the same sampling ports distributed equally along the length of the flow tube, but experiments displayed in panel (A-C) were performed with a total flow rate of 23.4 L min^{-1} (resulting in reaction times between 0.3 and 4.5 s), while experiments displayed in panel (D-F) were performed with a total flow rate of 10.7 L min^{-1} (resulting in reaction times between 0.5 and 7.7s). All experiments were performed under dry conditions, and size distributions are the

average of 3 to 8 replicates (error bars correspond to one standard deviation) for each reaction time. All size distributions were corrected for particle losses through the sampling lines. Total particle concentrations and geometric mean diameters as a function of reaction times are given in Fig. S12.

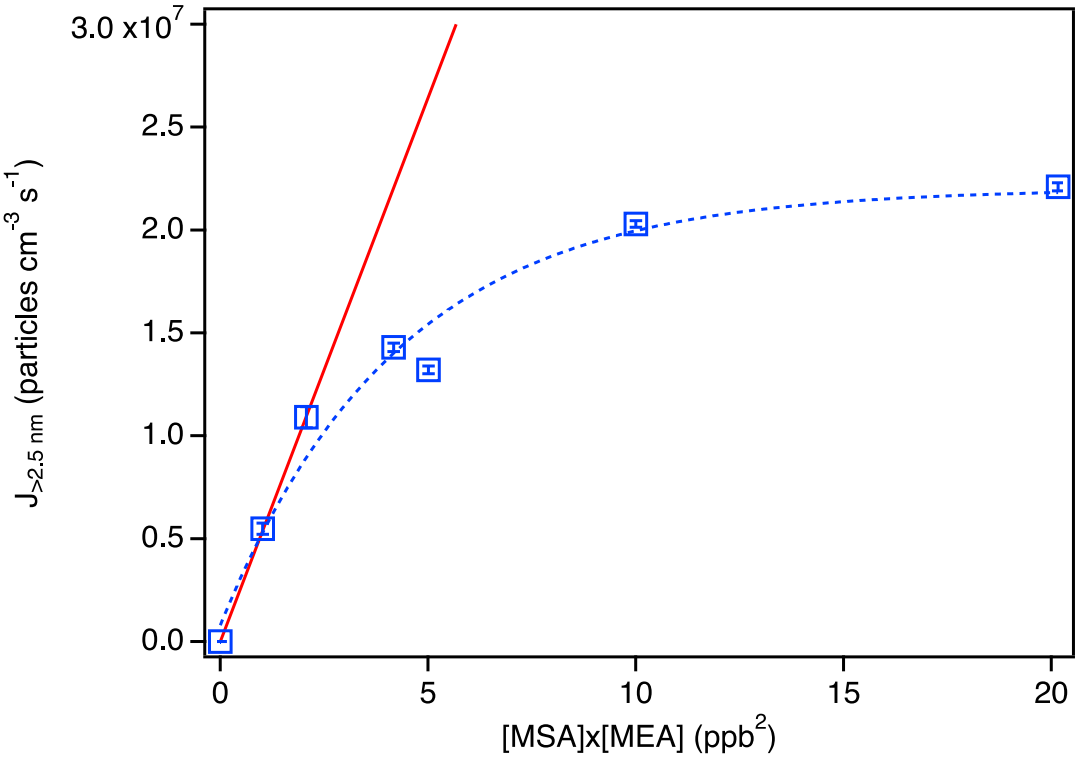

Figure 2. Particle formation rate ($J_{>2.5\ nm}$) for the MSA+MEA system under dry conditions as a function of the product of the MSA and MEA mixing ratios in ppb. Each data point represents an average over 3 to 8 individual SMPS scans taken at 2.3-2.4 s reaction time, with error bars representing one standard deviation, and corrected for particle losses through the sampling lines. The red line is a linear fit to the data ([MSA] $\times$ [MEA] $\leq$ 2 ppb^2) with a slope of (5.3 $\pm$ 0.03) $\times$ 10^6 particles cm^{-3} ppb^2.

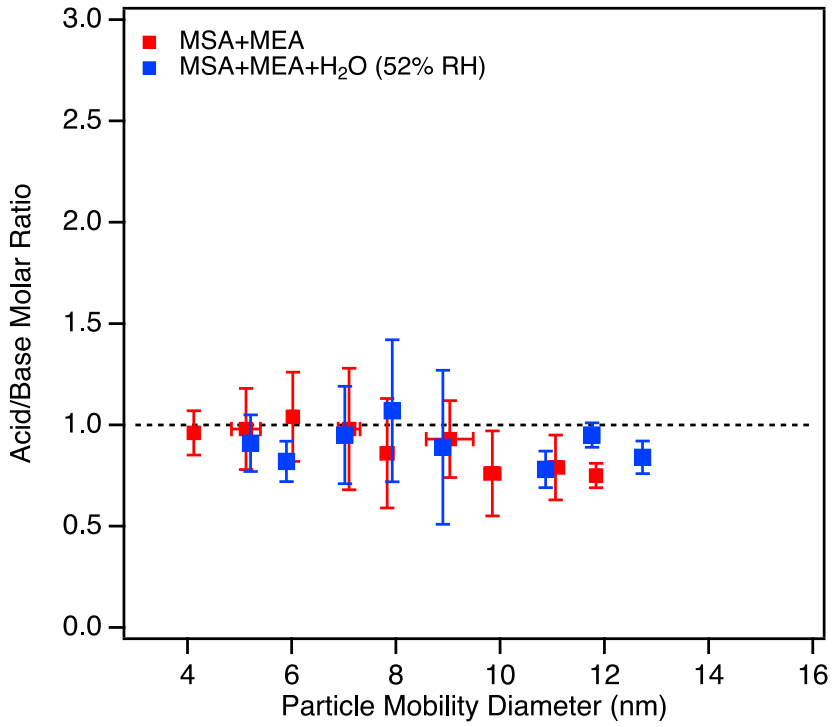

Figure 3. Acid/base molar ratio measured by the TDCIMS for the MSA+MEA system, under dry conditions (red data points) and at 52% RH (blue data points) measured at 4.5 s reaction time. MEA was measured in POS ion mode while MSA was measured in NEG ion mode, and the ion distributions in the MS spectra were similar at all reactant concentrations (Fig. S6). Text S5 provides more detailed information on how the acid/base molar ratios were estimated. All measurements were performed with initial MEA concentration of 1.5 ppb. No significant difference was observed in the measured molar ratio across for experiments performed with [MSA] = 0.68 ppb, [MSA] = 1.4 ppb or [MSA] = 2.8ppb, in either dry or humid conditions; thus the data points represent average values across the [MSA] concentrations range for each RH condition. For each data point, the error bars represent one standard deviation. The dashed line corresponds to an acid/base molar ratio of unity for reference.

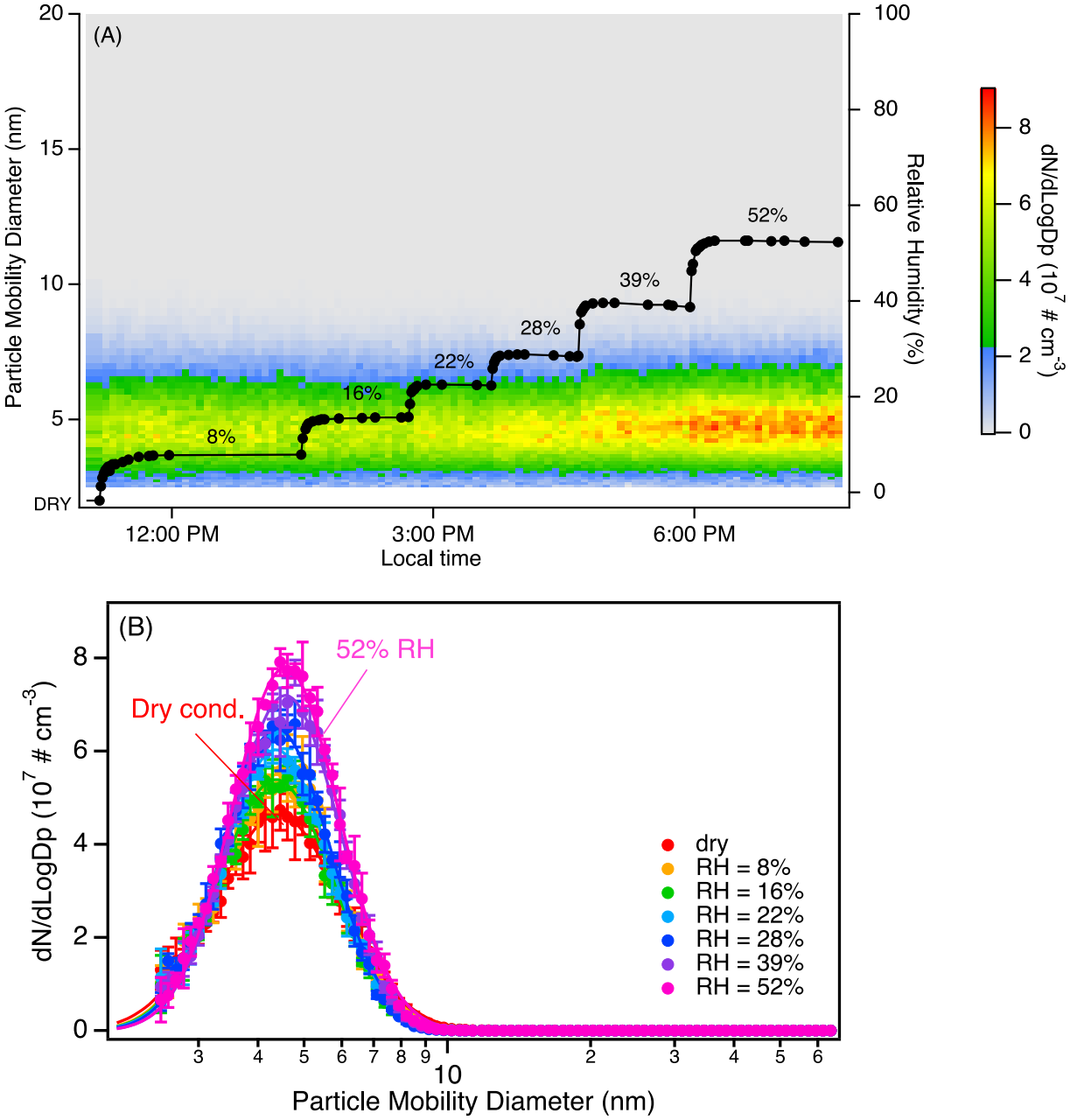

Figure 4. Evolution of the particle size distributions as a function of relative humidity (RH) from the reaction of MSA (0.7 ppb) with MEA (1.4 ppb). Panel (A) represents the evolution as a function of time while panel (B) represents a snapshot of the size distributions at a given RH (each distribution is an average over three SMPS scans with the error bars representing one standard variation). All measurements were performed at 4.5 s reaction time, and particle size distributions were corrected for particle loss through the sampling lines.

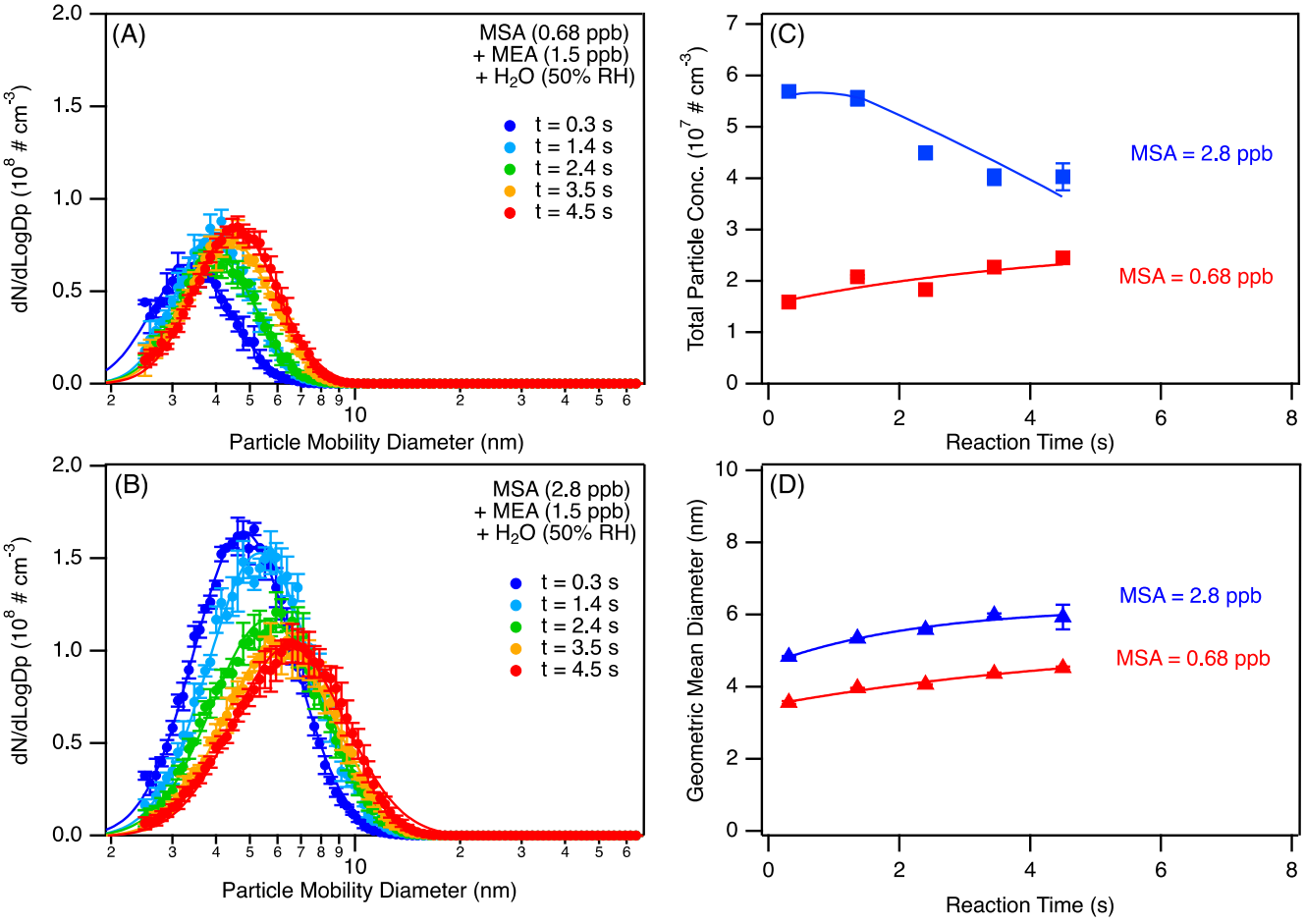

Figure 5. Size distributions (A and B) and evolution of the particle total concentrations and geometric mean diameters measured as a function of the reaction time (C and D) in the flow reactor for the MSA+MEA reaction system at 50% RH. All lines in panels C and D are guides to the eye. All data originate from replicate scans (n = 5) and are displayed with one standard deviation. All size distributions were corrected for particle losses through the sampling lines.

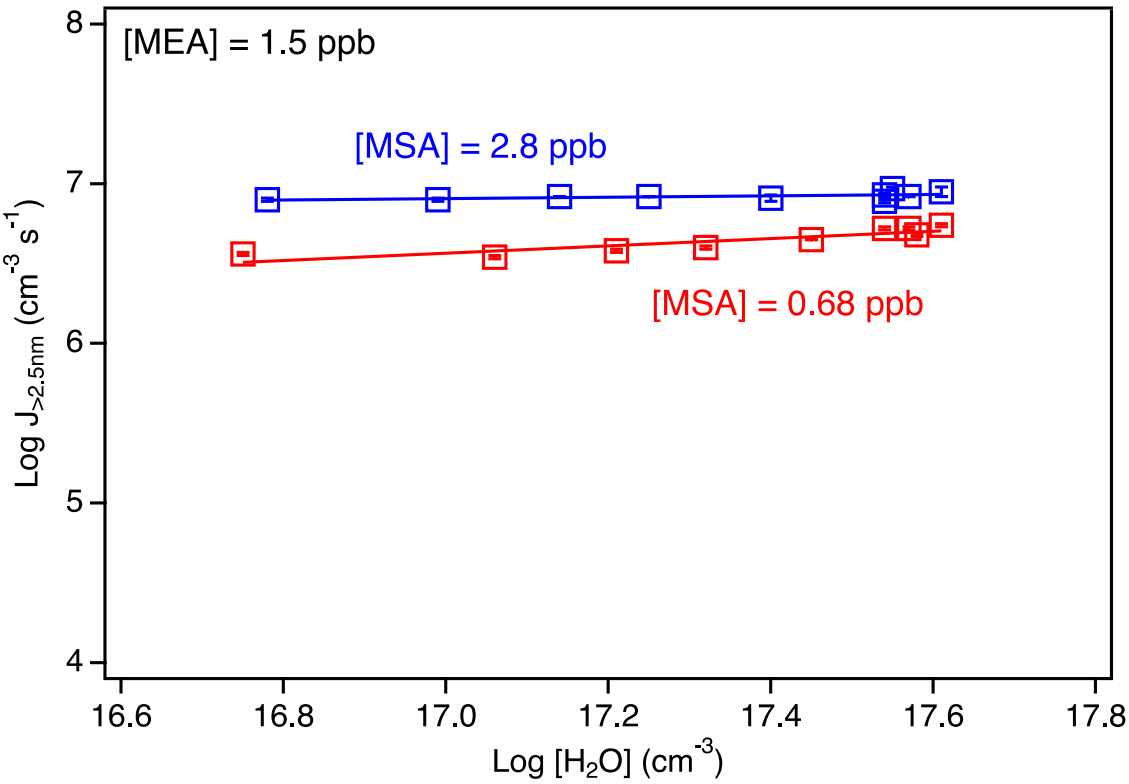

Figure 6. Logarithm of the particle formation rate ($J_{>2.5\ nm}$) for the MSA+MEA system under humid conditions (RH ranging from 8 to 56%) as a function of the log of the water concentration (in molecule cm^{-3}). Each data point represents an average over 3 to 6 individual SMPS scans taken at 4.5 s reaction time, with error bars representing one standard deviation. All data points were corrected for particle loss through the sampling line. Red data are for [MSA] = 0.68 ppb and [MEA] = 1.5 ppb while the blue data are for [MSA] = 2.8 ppb and [MEA] = 1.5 ppb. The slopes of the lines are 0.04 for 2.8 ppb MSA and 0.2 for 0.68 ppb MSA.

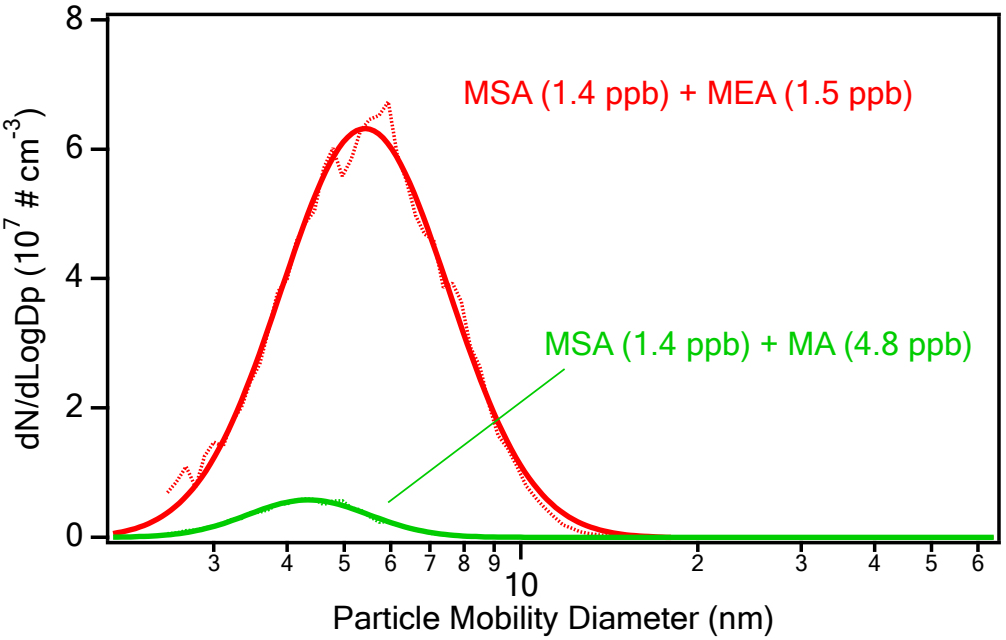

Figure 7. Representative averaged size distribution (red trace) from the reaction of MSA (1.4 ppb) with MEA (1.5 ppb). For comparison, a size distribution for MSA (1.4 ppb) reacting with MA (4.8 ppb) is also shown (green trace). Both size distributions were taken at ~4 s reaction time. Each size distribution was averaged over five consecutive scans and the shaded area corresponds to one standard deviation uncertainty. The thick line corresponds to a log normal fit to the averaged data. Both size distributions have been corrected for particle losses through the sampling lines.

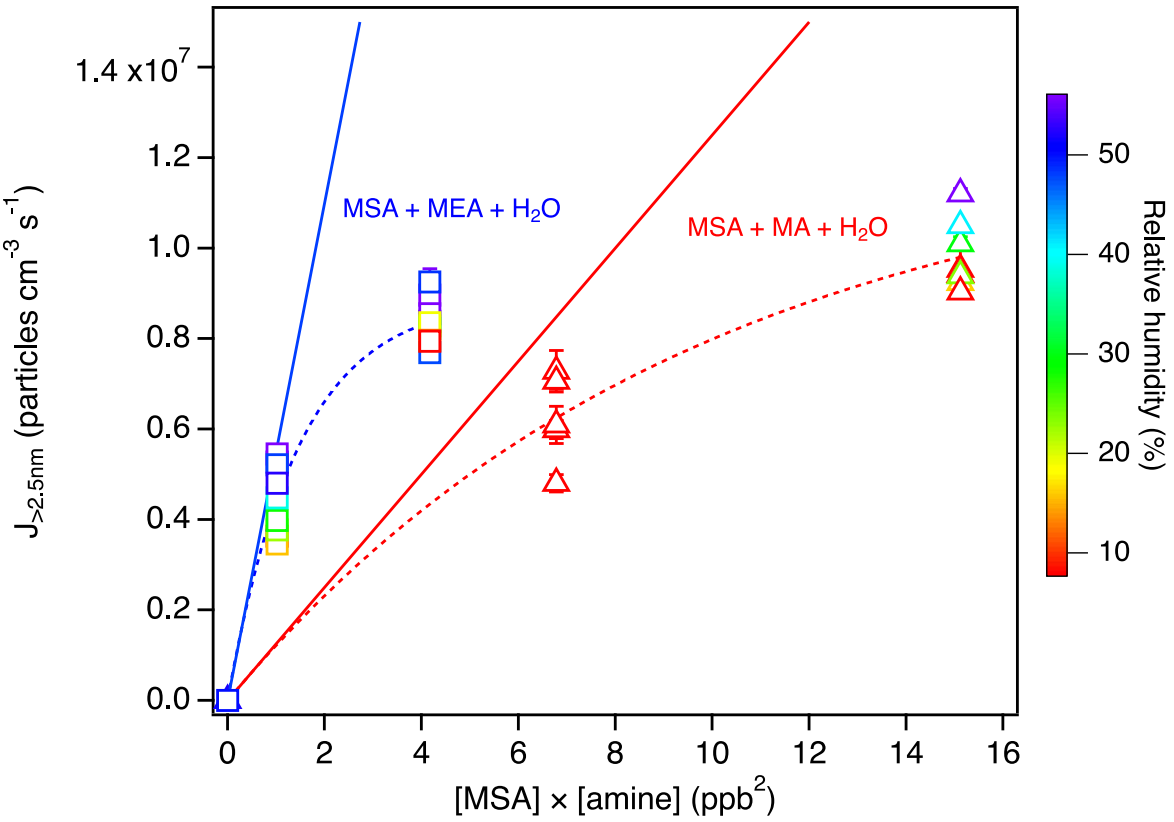

Figure 8. Comparison between particle formation rate ($J_{>2.5\ nm}$) for the MSA+MEA and the MSA+MA systems under humid conditions (RH ranging from 8 to 56%) as a function of the product of the MSA and the amine mixing ratios in ppb. Each data point represents an average over 3 to 6 individual SMPS scans taken at 4.5 s reaction time, with error bars representing one standard deviations. The dashed lines are exponential fits to the data and the solid lines are the tangent to the fits with slopes of 5.5×10^6 and 1.2×10^6 for the MSA+MEA and MSA+MA systems respectively. All data points were corrected for particle loss through the sampling lines.